

Data-driven discovery of high performance layered van der Waals piezoelectric NbOI₂

Yaze Wu^{1,2,9}, Ibrahim Abdelwahab^{2,5,9}, Ki Chang Kwon⁵, Ivan Verzhbitskiy^{1,2}, Lin Wang⁵,
Weng Heng Liew⁶, Kui Yao⁶, Goki Eda^{1,2}, Kian Ping Loh^{2,5,7*}, Lei Shen^{3,4*},
Su Ying Quek^{1,2,7,8*}

¹Department of Physics, National University of Singapore, Singapore, Singapore.

²Centre for Advanced 2D Materials and Graphene Research Centre, Singapore, Singapore.

³Department of Mechanical Engineering, National University of Singapore, Singapore, Singapore.

⁴Engineering Science Programme, National University of Singapore, Singapore, Singapore.

⁵Department of Chemistry, National University of Singapore, Singapore, Singapore.

⁶Institute of Materials Research and Engineering, A*STAR (Agency for Science, Technology and Research), Singapore.

⁷NUS Graduate School, Integrative Sciences and Engineering Programme, National University of Singapore, Singapore.

⁸Department of Materials Science and Engineering, National University of Singapore, Singapore.

⁹These authors contributed equally: Yaze Wu, Ibrahim Abdelwahab.

*e-mail: chmlhokp@nus.edu.sg; shenlei@nus.edu.sg; phyqsy@nus.edu.sg

Abstract

Using high-throughput first-principles calculations to search for layered van der Waals materials with the largest piezoelectric stress coefficients, we discover NbOI₂ to be the one among 2940 monolayers screened. The piezoelectric performance of NbOI₂ is independent of thickness, and its electromechanical coupling factor of near unity is a hallmark of optimal interconversion between electrical and mechanical energy. Laser scanning vibrometer studies on bulk and few-layer NbOI₂ crystals verify their huge piezoelectric responses, which exceed internal references such as In₂Se₃ and CuInP₂S₆. Furthermore, we provide insights into the atomic origins of anti-correlated piezoelectric and ferroelectric responses in NbOX₂ (X = Cl, Br, I), based on bond covalency and structural distortions in these materials. Our discovery that NbOI₂ has the largest piezoelectric stress coefficients among 2D materials calls for the development of NbOI₂-based flexible nanoscale piezoelectric devices.

Piezoelectric materials enable the interconversion between mechanical and electrical energy. This is made possible by the change in polarization of the material when it is stretched or compressed. As such, piezoelectric materials are integral components of intelligent, multi-functional devices and drive a multi-billion dollar industry¹ through their applications as sensors, actuators, energy harvesters, *etc.*²⁻⁷. The recent thrust toward flexible nanoscale devices creates a need for two-dimensional (2D) piezoelectric materials. Piezoelectric materials comprised of one or few layers of layered van der Waals (vdW) systems are particularly useful for increasingly important niche applications such as actuators with extreme atomic-scale precision⁸ as well as wearable sensors and smart material applications that require a large voltage signal in response to a small amount of physical deformation. 2D piezoelectric materials provide a practical alternative to micro-scale battery packs, functioning as nano-generators to power nanoscale devices⁹.

Thus far, the discovery of 2D piezoelectric materials has mostly been *ad hoc*, for example, by performing calculations on specific 2D materials that are known to be ferroelectric. However, with an *ad hoc* approach, it is difficult to ascertain if the 2D material indeed has optimal piezoelectric coefficients. Experimentally, it is also challenging to quantitatively compare the piezoelectric coefficients of 2D materials¹⁰. The objective of this work is to perform a systematic high throughput search through a 2D material database, in order to rank the 2D materials according to the size of their intrinsic piezoelectric coefficients. While 2D materials down to nanometres in thickness are sufficient for flexible nanoscale devices, symmetry-breaking in the monolayer can lead to the emergence of piezoelectricity in the monolayer even when the parent bulk materials are not piezoelectric¹¹. Thus, we focus our search on monolayers. Out of 109 piezoelectric monolayers that we identify, the family of niobium oxydihalides NbOX_2 ($X = \text{Cl}, \text{Br}, \text{I}$) is predicted to have among the largest in-plane piezoelectric stress coefficients, an order of magnitude larger than those of

most reported 2D materials. We note that NbOX₂ has recently been independently identified to be a robust room temperature ferroelectric in another high-throughput study searching for 2D ferroelectric materials¹². While all ferroelectric materials are piezoelectric, there is no direct correlation between the magnitude of spontaneous polarization $|\vec{P}|$ and the magnitude of piezoelectric coefficients (see [Supplementary Fig. S1](#)). Within the NbOX₂ family, our calculations in fact show that the piezoelectric and ferroelectric effects have opposing trends down the halogen group. We further show that the large piezoelectric effect is independent of crystal thickness, in contrast to MoS₂ and similar 2D in-plane piezoelectrics, where the piezoelectricity vanishes for an even number of layers¹³⁻¹⁵. This thickness-independent piezoelectric effect is a practical advantage in isolating 2D nanoscale piezoelectrics. Experimental validations of the piezoelectric effect were carried out on few-layer NbOI₂ and NbOCl₂ crystals, where significantly larger piezoelectric coefficients were obtained compared to internal references such as In₂Se₃ and CuInP₂S₆ (known 2D piezoelectrics)¹⁶⁻²⁰. Our findings pave the way for the development of NbOI₂-based flexible nanoscale piezoelectric devices, such as high precision actuators and wearable electronics or energy-harvesters.

Results and discussion

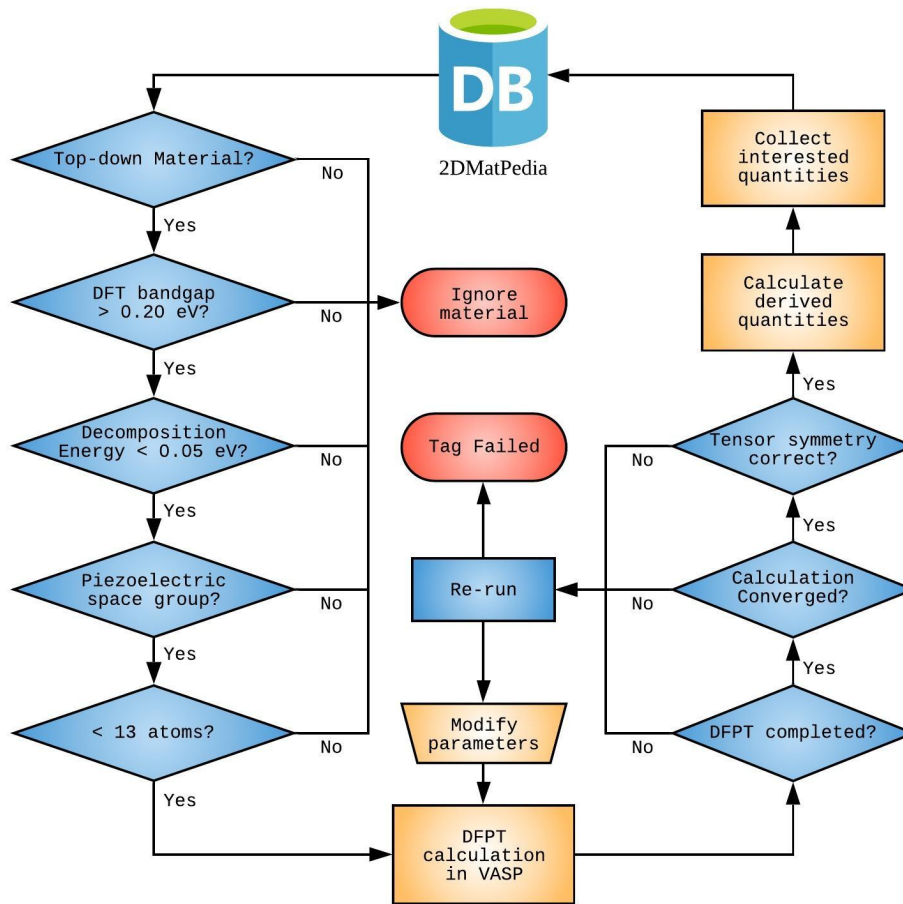


Fig. 1 | Workflow of the high-throughput calculation to screen for piezoelectric 2D materials. We have chosen a criteria of at least 0.20 eV for the DFT band gap (large enough for operation at finite temperatures) and a decomposition energy²¹ of < 0.05 eV to ensure thermodynamic stability.

The workflow of our high-throughput calculations is shown in [Fig. 1](#). Our results are publicly available in 2DMatpedia²¹, an open database of 2D materials that shares the same infrastructure and basic workflow as the Materials Project database²². We focus only on the 2940 “top-down” materials within the database, which are obtained by exfoliation of known bulk layered materials, and are more likely to be dynamically stable and

experimentally available. Next, we perform a rapid screening process based on the band gap and decomposition energy (both documented in 2DMatpedia²¹) as well as the space group (piezoelectric space groups lack inversion symmetry). A total of 225 materials pass this screening process. We then limit our high-throughput density functional perturbation theory (DFPT) calculations to materials with less than 13 atoms per unit cell (160 of the 225 materials). Following conventions for 2D materials, we compute the sheet piezoelectric stress tensor elements, e_{ij} , defined as $\frac{\partial P_i}{\partial \eta_j} L$, the rate of change in polarization P_i with homogeneous strain η_j multiplied by the cell height L ²³. The index i runs from 1 to 3 (x, y, z) and j ranges from 1 to 6 (xx, yy, zz, yz, xz, xy) where the Voigt notation is used. A series of automated checks and analyses is carried out and the relevant data is saved into the database. 51 materials did not pass the automated checks. This is similar in proportion to those in other high throughput studies^{1,24,25}; these materials were not studied in detail. The dynamical stability of individual materials is checked manually as needed outside this workflow.

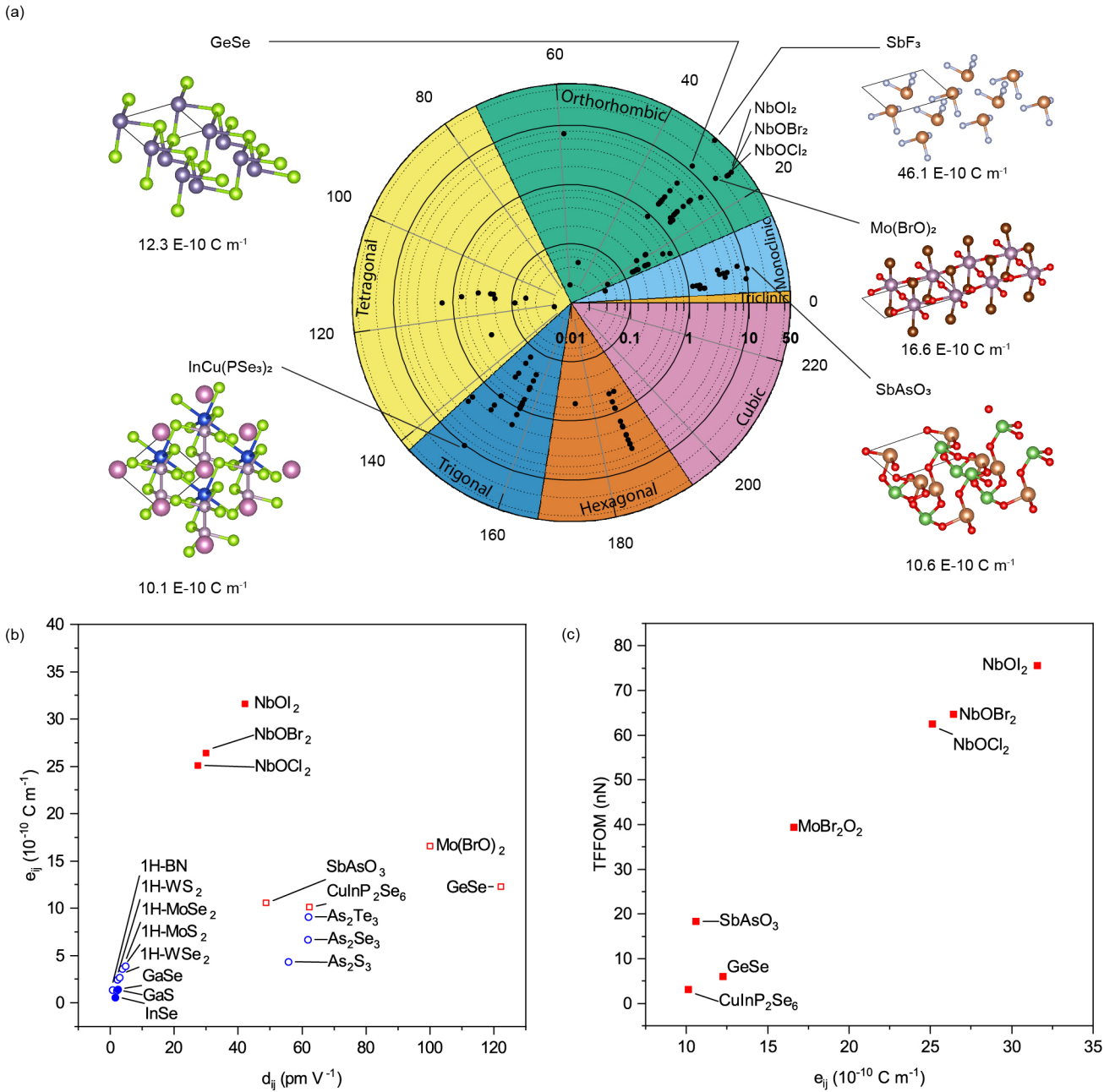


Fig. 2 | Maximum sheet piezoelectric tensor elements, thin film figure of merit (TFFOM) and spontaneous polarizations. (a) High-throughput calculation results for maximum sheet piezoelectric stress tensor elements (e_{ij}). The radial axis represents the magnitude of e_{ij} in units of $10^{-10} C m^{-1}$ on a log scale and the angular axis represents the 230 space groups. Materials with e_{ij} larger than $10 \times 10^{-10} C m^{-1}$ are labeled and their atomic structures are presented. The maximum e_{ij} corresponds to e_{26} for SbF_3 and to e_{11} for $NbOX_2$. **(b)** Plot of maximum sheet piezoelectric stress tensor elements (e_{ij}) and

corresponding piezoelectric strain tensor elements (d_{ij}) for various 2D materials. For additional notes on GeSe, please see [Supplementary Table S1](#). (c) Plot of TFFOM and maximum e_{ij} of materials highlighted in (a). In (b), solid symbols denote materials that are piezoelectric in the thermodynamically most stable bulk form, as documented in the Materials Project database¹; hollow symbols denote those that are not. Blue dots denote data points obtained from other studies^{17, 23, 26-28} listed in [Supplementary Table S2](#). Our computed e_{ij} values for these materials are also provided in [Supplementary Table S2](#) for comparison.

The final results are summarized in [Fig. 2a](#). All the 109 materials (see [Supplementary Table S15](#) for the full list) have an e_{ij} value greater than $0.05 \times 10^{-10} \text{ C m}^{-1}$. These 109 2D piezoelectric materials are observed to belong to only a few space groups ([Fig. 2a](#)). Space groups 17, 26, 31, 149, 156 and 187 each have more than nine 2D piezoelectric materials. Our high throughput calculations also found that 48 of the 109 2D piezoelectric materials are not ferroelectric (see [Supplementary Table S15](#)). 2D materials previously identified to be piezoelectric^{23, 26} are also found to be piezoelectric in our calculations, with values of e_{ij} very close to their reported values ([Supplementary Table S2](#)). Most materials have maximum e_{ij} values below $5 \times 10^{-10} \text{ C m}^{-1}$, while a few have significantly larger e_{ij} . These larger e_{ij} values correspond to in-plane piezoelectricity.

We identify eight materials with maximum sheet e_{ij} values larger than $10 \times 10^{-10} \text{ C m}^{-1}$, namely, SbF₃, NbOI₂, NbOBr₂, NbOCl₂, MoBr₂O₂, GeSe, SbAsO₃, CuInP₂Se₆. The structures of these eight materials (referred to as the ‘top 8’ materials) are presented in [Fig. 2a](#) and [Fig. 3](#). SbF₃, which has the largest sheet e_{ij} , is found to be dynamically unstable in the monolayer form. Niobium oxydihalides, NbOX₂, with X = Cl, Br, or I,

have the next highest sheet e_{ij} , with NbOI₂ having the largest e_{11} value of $\sim 32 \times 10^{-10} \text{ C m}^{-1}$. We have verified explicitly that monolayer NbOI₂ is dynamically stable ([Supplementary Fig. S2 and Fig. S3](#)) and we expect the same to be true for the other members of the family. The exfoliation energy for NbOI₂ monolayers is 18.2 meV \AA^{-2} , lower than that of graphene (25.5 meV \AA^{-2})²¹.

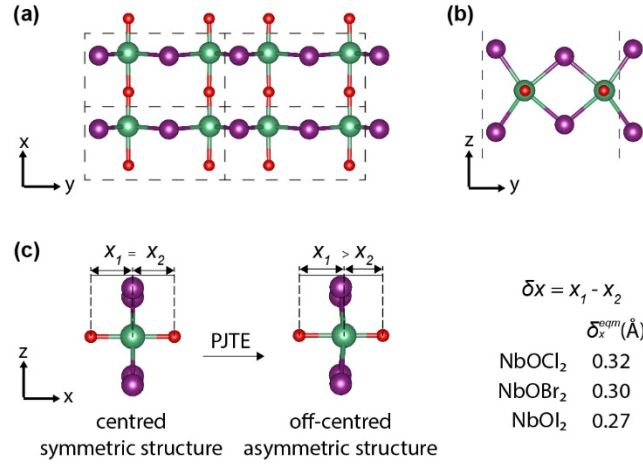


Fig. 3 | Atomic structure of monolayer NbOX₂ (X = I, Br, Cl). Dark green balls denote Nb atoms; purple balls denote halogens; red balls denote O atoms. Dashed lines mark the unit cell boundaries. (a) Top view. (b) Side view down the x -axis. (c) Schematic, viewed along y -axis, showing relative displacement of Nb atoms along the x -axis away from the high symmetry position where $\delta x = 0 \text{ \AA}$, to the equilibrium position where $\delta x = \delta x^{eqm}$. Additional structural parameters are provided in [Supplementary Table S3](#). PJTE refers to the pseudo-Jahn-Teller effect.

Besides the piezoelectric stress tensor elements e_{ij} , the piezoelectric strain tensor elements d_{ij} are also widely discussed in the literature. The d_{ij} values are defined as $\frac{\partial P_i}{\partial \sigma_j}$, the rate of change in polarization P_i with homogeneous stress σ_j (see SI), and are related to e_{ij} according to $d_{ij} = e_{ik} S_{kj}$, where S_{kj} is the compliance tensor (the inverse of the elastic

tensor). Unlike e_{ij} and S_{kj} which have a different definition for the 2D case, the d_{ij} values are defined in the same manner for both bulk and 2D (see Formalisms in SI). The d_{11} values for monolayer NbOX₂ are ~42, 30 and 27 $pm V^{-1}$ for NbOI₂, NbOBr₂ and NbOCl₂, respectively (see [Supplementary Table S4](#)). We note that all the d_{ij} values for bulk NbOX₂ are almost the same as for the monolayer ([Table 2](#) and [Supplementary Table S5](#)), indicating that the piezoelectric properties of NbOX₂ are very similar from monolayer to bulk form. In the bulk material, the ratio of mechanical stress energy density to the electrical energy density is given by a dimensionless number $k^2 = \frac{e_{ij}d_{ij}}{\epsilon_{ij}\epsilon_0}$ ^{29, 30}, where k is known as the electromechanical coupling factor. We obtain an electromechanical coupling factor of ~1.0, 0.9 and 0.9 for bulk NbOI₂, NbOBr₂ and NbOCl₂, respectively (see [Supplementary Table S5](#)). Since the maximum value of k is unity, we see that the intrinsic piezoelectricity in NbOX₂ provides for highly efficient interconversion between electrical and mechanical energy. Our many-body perturbation theory calculations³¹ predict a fundamental band gap of ~2.2 eV for monolayer NbOI₂, which is large enough for room temperature applications.

Table 1 | Materials with $e_{ij} > 10 \times 10^{-10} C m^{-1}$. e_{ij} is the piezoelectric stress tensor element, d_{ij} is the piezoelectric strain tensor element, C_{ij} is the elastic tensor element, and TFFOM is the figure of merit for thin film piezoelectric devices.²⁹ Our computed in-plane dielectric constant of NbOX₂ is 12 – 15 (see [Supplementary Table S6](#)).

Material	ij	e_{ij} ($10^{-10} C m^{-1}$)	d_{ij} ($pm V^{-1}$)	C_{ij} ($N m^{-1}$)	TFFOM (nN)
NbOI ₂	11	31.6	42.2	75.6	71.7
NbOBr ₂	11	26.4	30.0	89.0	63.2
NbOCl ₂	11	25.1	27.4	92.9	59.6
MoBr ₂ O ₂	22	16.6	100.1	33.8	39.3
GeSe	22	12.3	122.2	18.2	6.0
SbAsO ₃	11	10.6	48.7	22.3	18.4
CuInP ₂ Se ₆	22	10.1	62.3	44.5	3.1

Table 2 | Piezoelectric tensor elements and spontaneous polarizations of NbOX₂.

Sheet piezoelectric stress tensor elements e_{ij} are in units of 10^{-10} C m⁻¹ and piezoelectric strain tensor elements d_{ij} are in pm V⁻¹. Piezoelectric tensor elements that are zero due to symmetry of the space group are omitted here. Spontaneous polarization along the x -direction (P_x) in pC m⁻¹ is calculated as the difference between the polarization of the equilibrium and symmetric structures.

Formula	e_{11}	e_{12}	e_{13}	e_{26}	e_{35}	d_{11}	d_{12}	d_{26}	P_x
NbOCl ₂	25.1	-1.1	-0.4	0.8	0.0	27.4	-4.1	5.4	185
NbOBr ₂	26.4	-1.0	-0.4	0.8	0.0	30.0	-4.1	5.8	170
NbOI ₂	31.6	-1.0	-0.3	0.7	0.0	42.2	-5.1	5.2	143

We compute the d_{ij} values for the top 8 materials (excluding SbF₃) and the largest components of e_{ij} and d_{ij} are shown in **Fig. 2b** and **Table 1**. The maximum e_{ij} and d_{ij} values for other 2D piezoelectrics discussed in the literature are also plotted in **Fig. 2b** for comparison (see also **Supplementary Table S2**). Some materials such as monolayer GeSe²⁷, As₂S₃¹⁷, As₂Se₃¹⁷ have large d_{ij} values but small e_{ij} values, corresponding to small values of their Young's moduli. The small Young's moduli limits the amount of force exerted in electric field-induced deformations. (The 2D Young's moduli C_{11} for monolayer NbOI₂ is ~76 N/m (**Supplementary Table S7**) while the bulk value for C_{11} is ~125 GPa.) A figure of merit adopted for thin-film piezoelectrics (TFFOM), when the passive elastic layer is much thicker than the piezoelectric material, is $\frac{e_{ij}^2}{\epsilon_{ij}\epsilon_0}$, where ϵ_{ij} is the dielectric constant and ϵ_0 is the vacuum permittivity^{29, 32, 33}. Thus, the piezoelectric stress coefficients rather than the piezoelectric strain coefficients are particularly important for 2D flexible piezoelectric applications.

It is clear that NbOX₂ has the largest e_{ij} values in **Fig. 2b**. To our knowledge, there is only one 2D material, SnSe, with a predicted e_{11} value²⁷ that is larger than NbOI₂. Recent

experiments on SnSe have, however, reported a much weaker piezoelectric performance⁹ (see [Supplementary Table S8](#)), which we attribute to the Poisson effect, which reduces the effective e_{11} value of SnSe by ~51% (see [Supplementary Table S1](#)). We note that our high throughput calculations do not account for the Poisson effect. However, the Poisson effect does not change the e_{11} values for NbOX₂ (see [Supplementary Table S1](#)). The figure of merit (TFFOM) for our top 8 candidates from the high throughput calculations (except SbF₃) are presented in [Fig. 2c](#) and [Table 1](#), where it is clear that NbOI₂ has the largest TFFOM.

In [Fig. 2b](#), we also indicate using solid symbols the materials that are piezoelectric in the thermodynamically most stable bulk form, and hollow symbols for those that are not. NbOX₂ are among the minority of 2D materials that are piezoelectric both in the monolayer and in the bulk. The d_{ij} values are essentially the same for both monolayer and bulk NbOX₂ (see [Table S9](#)). Of the 109 piezoelectric materials that we discovered, only 30 are also piezoelectric in the bulk, according to a similar high throughput study¹ on the Materials Project database for bulk materials, from which the candidate monolayers were derived. A comparison of the largest e_{ij} values from the two independent studies indicates that the piezoelectric coefficients in the monolayer and the bulk are strongly correlated (see [Supplementary Table S10](#) and [Supplementary Fig. S4](#)). The thickness-independent piezoelectric effect in NbOX₂ implies that few-layer NbOX₂ can be prepared for nanoscale piezoelectric applications without the need for a pre-selection process based on the number of layers.

The atomic structure of monolayer NbOX₂ is shown in [Figs. 3a](#) and [3b](#). Along the y -direction, Peierls distortion results in alternating Nb-Nb distances, and along the x -direction, the Nb atom is displaced away from the high symmetry position where $\delta x = x_1 - x_2$ ([Fig. 3c](#)), giving rise to a spontaneous polarization ([Table 2](#)). The degree of

structural asymmetry along the x -direction is largest for NbOCl₂ and smallest for NbOI₂ (**Fig. 3c**). The asymmetry along the x -direction can be explained by the pseudo-Jahn-Teller effect (PJTE)³⁴, where mixing between the valence O p orbitals and conduction Nb d orbitals results in a more energetically favourable configuration accompanied by structural distortion as well as increased Nb-O bond strengths and covalency (see SI for details). The piezoelectric tensor elements in **Table 2** reflect the strong in-plane anisotropy of the system. In bulk NbOX₂, the directions for the inversion-symmetry-breaking distortions are the same in all layers, and the difference in δ_x^{eqm} is within 0.002 Å in the bulk and monolayer systems (**Supplementary Table S3** and **Table S11**). Thus, the piezoelectric properties are similar in bulk, monolayer and thin film form.

Quantitative measurements of piezoelectric coefficients in 2D materials are challenging, since any small parasitic vibration, boundary effect, or electrostatic force during the piezoelectric measurement (especially the single-point measurement) significantly affect the accuracy of the measured values¹⁰. To provide quantitative information about the piezoelectric coefficients within the family of NbOX₂, and to compare the piezoelectric coefficients with those of other known 2D piezoelectrics, α -In₂Se₃ and CuInP₂S₆, we performed laser scanning vibrometer (LSV)³⁵ measurements on thick bulk-like samples. All these materials are also piezoelectric in the bulk. The existence of ferroelectricity and piezoelectricity in thin films of NbOX₂ was demonstrated using piezoresponse force microscopy (PFM) for thicknesses down to sub-10 nm.

We synthesize large-sized NbOI₂ and NbOCl₂ crystals grown by the chemical vapor transport method (refer to Methods for details). The crystal structures of the as-grown NbOI₂ and NbOCl₂ crystals are confirmed by single-crystal X-ray diffraction (SC-XRD) (**Supplementary CIFs** and **Supplementary Table S11**). The crystallographic directions of the NbOX₂ crystals are also identified from the SC-XRD analysis. These room

temperature SC-XRD studies show that the crystal belongs to polar space group C2 (No. 5), hence providing further evidence that the ground state of bulk NbOX₂ is ferroelectric (refer to [Supplementary Note 1: Polarization switching in NbOX₂](#) and [Supplementary Note 2: Ferroelectric-paraelectric phase transition in NbOI₂](#) for ferroelectric data).

To investigate if ultrathin NbOX₂ is ferroelectric, nanosheets were exfoliated from bulk crystals via the Scotch tape method, and then transferred onto gold (Au) substrates ([Supplementary Fig. S5](#)) for PFM characterization. NbOX₂ is thermodynamically stable and all experimental measurements were performed under ambient conditions. In PFM, an AC voltage is applied between a conductive sharp tip and the bottom electrode of a piezoelectric sample to induce local mechanical deformations by means of the converse piezoelectric effect^{36, 37}. Scanning tip-induced hysteretic switching events were recorded using spectroscopic PFM ([Supplementary Note 1: Polarization switching in NbOX₂](#), and [Fig. S18](#)). The ferroelectric-paraelectric phase transition in NbOI₂ was further observed using temperature-dependent differential scanning calorimetry and second harmonic generation measurements ([Supplementary Note 2: Ferroelectric-paraelectric phase transition in NbOI₂](#), and [Fig. S19](#)).

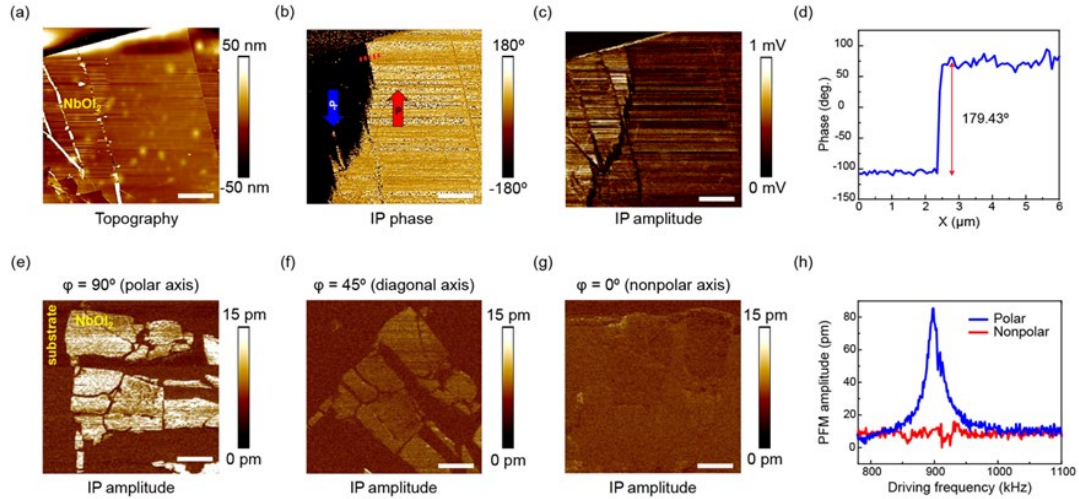


Fig. 4 | Piezoelectric force microscopy (PFM) investigation of thin NbOX₂. (a) Topography, (b) In-plane (IP) phase, (c) IP amplitude, and (d) phase profile across antiparallel polarization states of 82-nm-thick NbOI₂ flake. (e-g) Vector PFM IP amplitude images of 10-nm-thick NbOI₂ showing spontaneous polarization at 90° (e), 45° (f), and 0° (g) angles relative to the cantilever long axis. (h) PFM amplitude profiles along the polar and nonpolar axes of the 10-nm-thick NbOI₂ flake. Scale bars: 4 μm. Drive voltage: (b,c) 5 V, (e-h) 3 V. Drive frequency: (b,c) 65 kHz, (e) 827 kHz, (f) 974 kHz, (g) 890 kHz.

Figs. 4b and **4c** present phase and amplitude images constructed by in-plane (IP) PFM output channel from 82-nm-thick NbOI₂ flake (**Fig. 4a**). A clear contrast exists between different domains in the lateral phase and amplitude. The PFM phase indicates the direction of the ferroelectric polarization, whereas the PFM amplitude reflects the magnitude of the local piezoelectric response. The bright and dark contrasts in the PFM phase image indicate that there exist two oppositely polarized ferroelectric domains, characterized by a ~180° phase difference (**Fig. 4d**). **Supplementary Fig. S6-Fig. S10** display additional PFM data for NbOI₂ and NbOCl₂, demonstrating piezoelectric response down to 4.3 nm-thickness for NbOI₂.

To confirm the in-plane piezoelectric anisotropy, vector PFM^{38, 39} is conducted on 10-nm-thick NbOI₂ (**Fig. 4e-h**) and 17-nm-thick NbOCl₂ (**Supplementary Fig. S11**) flakes with height profiles shown in **Supplementary Fig. S12**. As expected, the in-plane PFM response is strongest when the polar axis is orthogonal to the cantilever long axis, as shown in **Fig. 4e** (φ is the polarization angle relative to the cantilever long axis). When the sample is rotated by 90 degrees, no lateral PFM contrast is observed (**Fig. 4g, h**). In addition, the out-of-plane piezoresponses for the NbOX₂ nanoflakes are typically negligible, as displayed in **Supplementary Fig. S6-Fig. S10**. The vector PFM results as well as predominantly in-plane response confirms that the physical origin of the PFM signals is piezoelectricity rather than electrostatic tip-sample interactions^{40, 41}.

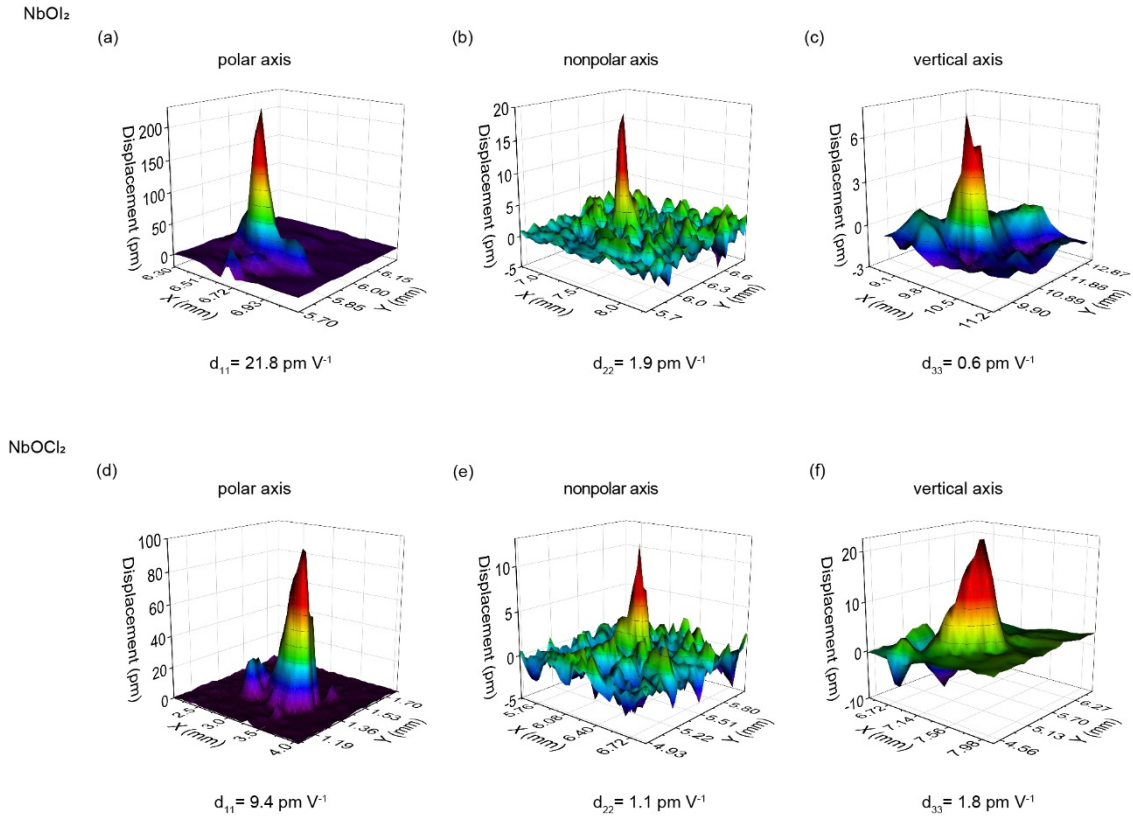


Fig. 5 | Evaluation of the piezoelectric coefficients of NbOX₂ using a laser scanning vibrometer (LSV). 3D graphs of the instantaneous vibration when the displacement magnitude reaches the maximum under the sine-wave driving electrical signal. **(a,d)** Measurement along the lateral polar direction (d_{11}). **(b,e)** Measurements along the lateral nonpolar direction (d_{22}). **(c,f)** Measurements along the vertical nonpolar direction (d_{33}).

We quantified the lateral (d_{11} , d_{22}) and vertical (d_{33}) piezoelectric coefficients of NbOX₂ through laser scanning vibrometer (LSV)³⁵ measurements. LSV is a non-contact optical technique that measures the vibration velocity of a moving piezoelectric surface by monitoring the interference pattern (Doppler frequency shift) between the scattered light and the incident light. By integrating the vibration velocity, the mechanical displacement in response to an applied electric field can be determined. Consistent with the vector PFM data, the LSV vibration modalities (**Fig. 5**) further confirm the anisotropy of the

piezoelectric response in NbOX₂. Our measurements reveal that NbOI₂ exhibits stronger piezoelectric effects than NbOCl₂ (the $\mathbf{d}_{11(eff)}$ values are ~ 21.8 pm V⁻¹ for NbOI₂ and ~ 9.4 pm V⁻¹ for NbOCl₂), consistent with our theoretical predictions (**Table 2**). These values are likely to be underestimated due to the significant electric leakage of the NbOX₂ samples. Despite this, our measured $\mathbf{d}_{11(eff)}$ piezoelectric coefficients are larger than the largest $\mathbf{d}_{ij(eff)}$ values we measured for common 2D ferroelectrics, such as α -In₂Se₃ and CuInP₂S₆ (**Supplementary Fig. S13**). There is also a strong correlation between the measured $\mathbf{d}_{ij(eff)}$ values and the corresponding computed values (**Supplementary Fig. S14**). These LSV results show that NbOX₂ has superior piezoelectric performance compared to other 2D material piezoelectrics.

We analyse the origins of the large piezoelectric and ferroelectric effects in NbOX₂, and their trends down the halogen group. The large values of \mathbf{e}_{11} arise predominantly from the lattice response to the applied strain (see **Supplementary Table S12**). This dominant ionic contribution can be written in an implied sum notation as

$$\mathbf{e}_{ij}^{ion} = \mathbf{Z}_{m,i}^* \frac{\partial \mathbf{u}_m}{\partial \eta_j} \quad 1$$

where $\mathbf{Z}_{m,i}^*$ is the dynamical charge (m is a composite label for atom and displacement direction and i is the direction of the polarization), \mathbf{u} is the position vector of the atom and η_j denotes the applied strain. The dynamical charge is defined as the rate of change of polarization with atomic displacement, while $\frac{\partial \mathbf{u}_m}{\partial \eta_j}$ quantifies the rate of change in atomic displacement with applied strain. The dynamical charges play an important role in both the piezoelectric and ferroelectric effects.

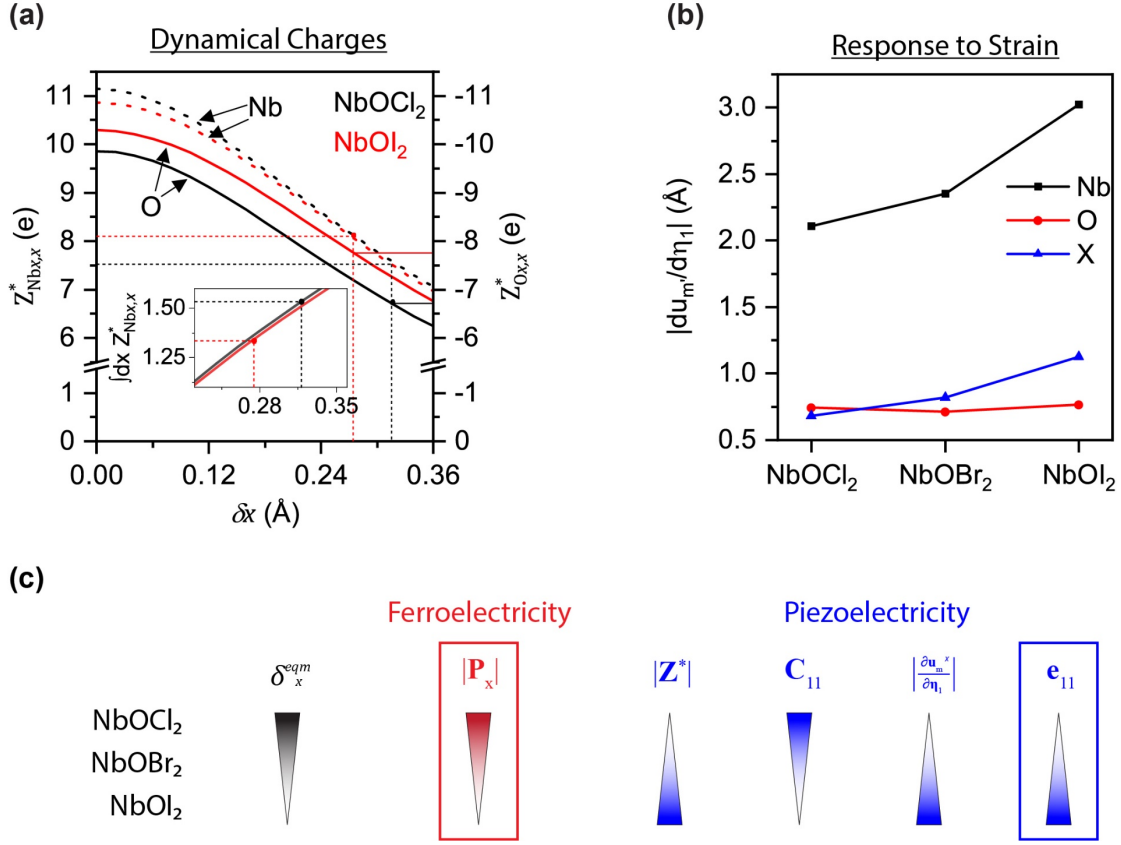


Fig. 6 | Understanding the origin of piezoelectric and ferroelectric effects in the NbOX₂ family. (a) Dynamical charges for Nb and O, $Z_{Nb,x,x}^*$ and $Z_{O,x,x}^*$, as a function of δx , the difference between the longer and shorter Nb-O bonds. The inset shows the integral of $Z_{Nb,x,x}^*$ with respect to the x -displacement away from the high-symmetry site. In both the main figure and the inset, dashed lines indicate the values in the equilibrium structures. (b) $|\frac{\partial u_m^x}{\partial \eta_1}|$ in the equilibrium structures of NbOX₂, indicating the rate of change of x -displacement of each atom (Nb, O or X) with strain in the x -direction. NbOI₂ has the largest lattice response to strain, due to the smaller stiffness tensor elements and weaker Nb-O bonds. (c) Schematic illustrating the origins for the trends in ferroelectricity and piezoelectricity in NbOX₂. In (a) and (b), the respective values for NbOBr₂ are between those of NbOCl₂ and NbOI₂, and are not shown here.

Fig. 6a shows that the dynamical charges in the x -direction for Nb and O in NbOCl₂ and NbOI₂, decrease in magnitude as the off-centre displacement, δx , increases. These dynamical charges are significantly larger in magnitude than their expected formal oxidation states (+4 for Nb and -2 for O) as well as their estimated static charges (see **Supplementary Fig. S15**). The anomalous dynamical charges can be attributed to the partial covalency present in the Nb-O bonds, which is more significant in NbOI₂ due to the smaller electronegativity of I compared to Cl (see SI and **Supplementary Fig. S16**)⁴². The smaller off-centre distortion in NbOI₂ (smallest δ_x^{eqm}) further increases the dynamical charges at equilibrium compared to those for NbOCl₂, contributing to the superior piezoelectric performance of NbOI₂. On the other hand, the integral of the dynamical charges with respect to atomic displacements, from the centred symmetric structure to the equilibrium off-centred structure, gives the magnitude of the spontaneous polarization at equilibrium, and the larger δ_x^{eqm} for NbOCl₂ results in a larger $|\vec{P}|$ compared to NbOI₂ (**Fig. 6a** inset).

The larger magnitudes of $\frac{\partial u_{mx}}{\partial \eta_1}$ (the superscript for m representing displacements in the x -direction) for Nb and X atoms in NbOI₂ (**Fig. 6b**) further contribute to the large e_{11} value for NbOI₂ (see also **Supplementary Table S13**). The observed trend in $\frac{\partial u_{mx}}{\partial \eta_1}$ for Nb and X can be traced to the degree of bond covalency/ionicity in these systems, the more ionic NbOCl₂ having stiffer bonds and hence smaller magnitudes of $\frac{\partial u_m}{\partial \eta_j}$. This trend can also be observed in the decrease in Young's modulus C_{11} down the halogen group (see **Supplementary Table S7**). **Fig. 6c** summarizes the different factors that contribute to e_{11} being largest for NbOI₂, in contrast to $|\vec{P}|$ being largest for NbOCl₂.

While our top candidates for monolayer piezoelectrics all exhibit in-plane piezoelectricity, we comment that out-of-plane piezoelectricity (non-zero e_{3j}) in the 2D monolayers is

found in 46 of the materials in our database, as shown in [Supplementary Fig. S17](#). Most of the non-zero e_{3j} values have magnitudes less than $1 \times 10^{-10} \text{ C m}^{-1}$, with a few exceptions having values up to $\sim 4 \times 10^{-10} \text{ C m}^{-1}$, as indicated in [Supplementary Fig. S17](#) and [Supplementary Table S14](#). It has been reported that bulk layered CuInP_2S_6 has an electromechanical coupling factor of 0.7-0.9, corresponding to a large out-of-plane piezoelectric coefficient which originates from the deformation of the van der Waals gap⁴³. Such a mechanism has not been considered in our study on monolayers. Our findings that monolayer and bulk NbOI_2 have exceptionally large in-plane piezoelectric effects are especially important for actuator applications that require pure in-plane movement⁴⁴.

In summary, we have identified, from among 2940 candidate monolayers, NbOI_2 as the material with the largest piezoelectric stress coefficient. Furthermore, NbOI_2 is one of the minority of monolayer piezoelectrics that is also piezoelectric in the bulk, with thickness-independent piezoelectric coefficients. Our experimentally measured values of piezoelectric strain coefficients are within a factor of two of the predicted value for NbOI_2 , and are much larger than those measured concurrently for $\alpha\text{-In}_2\text{Se}_3$ and CuInP_2S_6 . We have also verified in-plane ferroelectricity in NbOI_2 . While NbOI_2 has the largest piezoelectric coefficients, NbOCl_2 has the largest spontaneous polarization. The excellent piezoelectric and ferroelectric effects in NbOX_2 , as well as their trends down the halogen group, are rationalized on the basis of bond covalency and symmetry-breaking structural distortions in these materials. The structure-property correlations obtained here provide guidance for the design of functional piezoelectric and ferroelectric materials, while the discovery of 2D NbOI_2 as a high-performance piezoelectric paves the way for 2D piezoelectric devices.

Methods

Computational methods. For the high-throughput DFPT calculations, only materials from space groups 1, 3-9, 16-46, 75-82, 89-122, 143-146, 149-161, 168-174, 177-190, 195-199, 207-220¹ are selected. These space groups lack inversion symmetry. DFPT calculations are performed with the plane-wave pseudopotential code VASP^{45, 46}, employing the generalized gradient approximation (GGA) for the exchange-correlation functional⁴⁷. We use an energy cutoff of 520 eV, a Monkhorst-Pack k-point mesh with a density of 1500 per reciprocal atom (number of atoms per cell multiplied by the number of k-points)¹, a force convergence criterion of 0.005 eV/Å and a criterion of 10⁻¹⁰ eV for the convergence of the self-consistent cycle. The calculations are performed with a vacuum separation of about 20 Å between the 2D materials.

We modify the standard workflows^{48, 49} developed by Materials Project^{1, 22} to include additional post processing steps that convert the 3D piezoelectric tensor elements to 2D sheet piezoelectric tensor elements in the unit of C m⁻¹ by multiplying the former with the cell height. Other results, including the dynamical charge tensor (also known as the Born effective charge tensor), dielectric tensor (ionic and electronic contributions), Γ point phonon eigenvalue and eigenvectors, full piezoelectric tensor (in both C m⁻² and C m⁻¹), maximum (sheet) piezoelectric tensor elements in C m⁻² (C m⁻¹) and maximum (sheet) out-of-plane piezoelectric tensor elements in C m⁻² (C m⁻¹) are also captured. Our workflow also inherits the consistency checks and filters in the Materials Project Workflow¹ to detect errors arising from DFT calculation and convergence-related issues.

For the targeted study on NbOX₂, Monkhorst-Pack k point meshes of 12×6×1 including the Γ point are used. The atomic coordinates are fully relaxed using the conjugate gradient scheme until the maximum energy difference between iterations is less than 10⁻⁸ eV and

the residual force is less than 0.001 eV/Å. Other parameters are inherited from the high-throughput calculations.

For calculations with fixed δx , the x -coordinates of the atomic positions are fixed while the y and z coordinates are allowed to relax. The lattice constants are kept fixed. $\frac{\partial u_m^x}{\partial \eta_1}$ is obtained by applying strain in the x -direction and allowing the atoms to relax.

The elastic properties of NbOX₂ are obtained using a finite difference method as implemented in VASP. The elastic tensors are adapted for 2D materials according to the treatment by Choudhary et al.⁵⁰.

The piezoelectric strain tensor (\mathbf{d}_{ij}) is calculated from piezoelectric stress tensor (\mathbf{e}_{ij}) through [Supplementary Equation S7](#). Elements in \mathbf{S}_{ij} related to the z -direction are set to 0.

Synthesis of single crystals of NbOI₂ and NbOCl₂. Crystalline NbOI₂ and NbOCl₂ are grown by the chemical vapor transport method. High-purity Nb (film), iodine (crystals) and Nb₂O₅ (powder) with a stoichiometric ratio Nb:O:I = 1:1:2 are used as precursors for the growth of NbOI₂. The mixture of precursors is placed in a quartz ampule, and the ampule is sealed after being evacuated (10⁻⁵ Torr). Similarly, Nb, NbCl₅ (powder) and Nb₂O₅ are used to grow NbOCl₂. The sealed quartz ampules are placed at the centre of a horizontal dual-zone furnace. Both heating zones were slowly heated to 600 °C and holding for 5 days. The ampules are then slowly cooled for 10 days with slightly different rates at the hot (1.2 °C/hour) and cold (1.5 °C/hour) zones. After the slow-cooling process, the furnace is turned off allowing the ampules to cool down naturally. Crystals are extracted from the opened ampules under inert conditions of an N₂-filled glove box and then stored for future use.

X-ray diffraction (XRD) measurements. Single crystal X-ray diffractions of bulk NbOCl₂ and NbOI₂ crystals are measured using a four circles goniometer Kappa geometry, Bruker AXS D8 Venture, equipped with a Photon 100 CMOS active pixel sensor detector. A molybdenum monochromatized ($\lambda = 0.71073 \text{ \AA}$) X-Ray radiation is used for the measurement. The frames are integrated with the Bruker SAINT software using a narrow-frame algorithm. Data is corrected for absorption effects using the Multi-Scan method (SADABS). The structures are solved in the monoclinic unit cell and refined using the SHELXT, VERSION 2014/5 Software. The final anisotropic refinement of the structures is performed by least squares procedures on weighted F^2 values using the SHELXL-2014/7 (Sheldrick, 2014) included in the APEX3 v2016, 9.0, AXS Bruker program.

Sample preparation and piezoresponse force microscopy (PFM) characterization.

Mechanical exfoliation is performed by peeling off as-grown crystals using the Scotch tape method. Exfoliated crystals are directly transferred onto fresh gold (Au) substrates for PFM characterization. PFM images are obtained using a Bruker Dimension Icon AFM in contact mode. Pt/Ir-coated silicon tips with a radius of 20 nm and a force constant of 0.4 N/m are used for the PFM measurements. The drive frequency and drive amplitude for the PFM images are ~30-975 kHz and 2.5-10 V, respectively. The PFM amplitude is expressed in pm or mV units depending on the selected PFM output channel. Angular-resolved vector PFM was performed by rotating the NbOX₂ samples with respect to the cantilever axis.

Laser scanning vibrometer (LSV) measurements. The effective piezoelectric coefficients of NbOX₂, α -In₂Se₃, and CuInP₂S₆ (CIPS) are measured with a laser scanning vibrometer (OFV- 3001-SF6, PolyTech GmbH) after the crystals are DC poled under 150 V along the relevant crystallographic direction for 5 minutes. The LSV data are collected along the x (d_{11}), y (d_{22}) and z (d_{33}) directions of NbOX₂ and along the z (d_{33}) directions of

α -In₂Se₃ and CIPS under a unipolar AC signal of amplitude 10 V at 8 kHz through silver electrodes. The α -In₂Se₃ and CuInP₂S₆ crystals were purchased from HQGraphene. The effective piezoelectric coefficients are deduced from the profile analysis of the instantaneous displacement data to determine the strain generated under the sine-wave driving electrical signal.

Differential scanning calorimetry (DSC) analysis was performed under a nitrogen atmosphere with a heating rate of 10 °C/min using Mettler-Toledo DSC.

The polarization–electric field (P–E) curve was recorded using a ferroelectric tester (Precision Multiferroic II, Radiant Technologies).

Mechanical exfoliation is performed by peeling off as-grown crystals using the Scotch tape method. Exfoliated crystals are directly transferred onto fresh gold (Au) substrates for PFM characterization. PFM images are obtained using a Bruker Dimension Icon AFM in contact mode. Pt/Ir-coated silicon tips with a radius of 20 nm and a force constant of 0.4 N/m are used for the PFM measurements. The drive frequency and drive amplitude for the PFM images are ~30-975 kHz and 2.5-10 V, respectively. The PFM amplitude is expressed in pm or mV units depending on the selected PFM output channel. Angular-resolved vector PFM was performed by rotating the NbOX₂ samples with respect to the cantilever axis. The spectroscopic PFM hysteresis loops were acquired with ± 10 V DC sweeps while applying an AC voltage of 5 V.

Acknowledgements

Y.W. acknowledges support from the NUS Research Scholarship. K.Y and W.H.L. acknowledge partial support from the National Research Foundation, under the Competitive Research Programme of Singapore, NRF-CRP15-2015-04, and A*STAR, under RIE2020 AME Individual Research Grant (IRG) (Grant No.: A20E5c0086). G.E. acknowledges support from the Singapore MOE (Grant No. MOE2018-T3-1-005). L.S. acknowledges support from the Singapore MOE (Grant No. R-265-000-691-114 and MOE2019-T2-2-030, respectively). K. P. L. acknowledges funding from A*STAR AME-IRG program (Grant No: A1983c0035). Y.W., I.A., I.V., G.E., K.P.L. and S.Y.Q. acknowledge support from the Singapore National Research Foundation, Prime Minister's Office, under its medium-sized centre program. Y.W. acknowledges technical help from Miguel Dias Costa and Jun Zhou. Computations were performed on the NUS CA2DM computational cluster and National Supercomputing Centre Singapore. The authors would like to thank Yuan Ping Feng for his comments on the manuscript.

Author Contributions

S.Y.Q. and L.S. conceived the project. S.Y.Q. led the collaborative effort and direction of the project, and provided guidance on the theoretical analysis and calculations. L.S. provided guidance on the high-throughput piezoelectric calculations. Y.W. performed the calculations and theoretical analysis. I.A. designed the experiments and performed micromechanical cleavage, device fabrication and material characterization under the supervision of K.P.L.. K.C.K, L.W. and I.A. performed the PFM measurements. I.V. synthesized the NbOX₂ bulk crystals under the supervision of G.E.. W.H.L performed the LSV measurements under the guidance of K.Y., and both analysed the results. Y.W., I.A. and S.Y.Q. wrote the manuscript. All authors read and commented on the manuscript.

Competing Interests

The authors declare no competing interests.

Data Availability Statement

The datasets generated during and/or analysed during the current study are available from the corresponding author on reasonable request.

References

1. de Jong M, *et al.* A database to enable discovery and design of piezoelectric materials. *Scientific Data* 2015, **2**(1): 150053.
2. Gullapalli H, *et al.* Flexible Piezoelectric ZnO–Paper Nanocomposite Strain Sensor. *Small* 2010, **6**(15): 1641-1646.
3. Wang X, *et al.* Piezoelectric Field Effect Transistor and Nanoforce Sensor Based on a Single ZnO Nanowire. *Nano Lett* 2006, **6**(12): 2768-2772.
4. Doll JC, Peng AW, Ricci AJ, Pruitt BL. Faster than the Speed of Hearing: Nanomechanical Force Probes Enable the Electromechanical Observation of Cochlear Hair Cells. *Nano Letters* 2012, **12**(12): 6107-6111.
5. Yun Y, *et al.* A Multi-Wall Carbon Nanotube Tower Electrochemical Actuator. *Nano Lett* 2006, **6**(4): 689-693.
6. Romano G, *et al.* Piezoelectric potential in vertically aligned nanowires for high output nanogenerators. *Nanotechnology* 2011, **22**(46): 465401.
7. Wang ZL, Song J. Piezoelectric Nanogenerators Based on Zinc Oxide Nanowire Arrays. *Science* 2006, **312**(5771): 242-246.
8. Wang X, *et al.* Subatomic deformation driven by vertical piezoelectricity from CdS ultrathin films. *Science Advances* 2016, **2**(7): e1600209.
9. Li P, *et al.* A self-powered 2D-material sensor unit driven by a SnSe piezoelectric nanogenerator. *Journal of Materials Chemistry A* 2021, **9**(8): 4716-4723.
10. Chen QN, Ou Y, Ma F, Li J. Mechanisms of electromechanical coupling in strain based scanning probe microscopy. *Applied Physics Letters* 2014, **104**(24): 242907.
11. Hinchet R, Khan U, Falconi C, Kim S-W. Piezoelectric properties in two-dimensional materials: Simulations and experiments. *Materials Today* 2018, **21**(6): 611-630.
12. Jia Y, *et al.* Niobium oxide dihalides NbOX₂: a new family of two-dimensional van der Waals layered materials with intrinsic ferroelectricity and antiferroelectricity. *Nanoscale Horizons* 2019, **4**(5): 1113-1123.
13. Zhu H, *et al.* Observation of piezoelectricity in free-standing monolayer MoS₂. *Nature Nanotechnology* 2015, **10**(2): 151-155.
14. Esfahani EN, *et al.* Piezoelectricity of atomically thin WSe₂ via laterally excited scanning probe microscopy. *Nano Energy* 2018, **52**: 117-122.
15. Ares P, *et al.* Piezoelectricity in Monolayer Hexagonal Boron Nitride. *Advanced Materials* 2020, **32**(1).
16. Zhou Y, *et al.* Out-of-Plane Piezoelectricity and Ferroelectricity in Layered alpha-In₂Se₃ Nanoflakes. *Nano Letters* 2017, **17**(9): 5508-5513.

17. Gao W, Chelikowsky JR. Prediction of Intrinsic Ferroelectricity and Large Piezoelectricity in Monolayer Arsenic Chalcogenides. *Nano Letters* 2020, **20**(11): 8346-8352.
18. Ding W, *et al.* Prediction of intrinsic two-dimensional ferroelectrics in In₂Se₃ and other III₂-VI₃ van der Waals materials. *Nature Communications* 2017, **8**(1): 14956.
19. Liu F, *et al.* Room-temperature ferroelectricity in CuInP₂S₆ ultrathin flakes. *Nature Communications* 2016, **7**(1): 12357.
20. Cui C, Xue F, Hu W-J, Li L-J. Two-dimensional materials with piezoelectric and ferroelectric functionalities. *npj 2D Materials and Applications* 2018, **2**(1): 18.
21. Zhou J, *et al.* 2DMatPedia, an open computational database of two-dimensional materials from top-down and bottom-up approaches. *Scientific Data* 2019, **6**(1): 86.
22. Jain A, *et al.* Commentary: The Materials Project: A materials genome approach to accelerating materials innovation. *APL Materials* 2013, **1**(1): 011002.
23. Li W, Li J. Piezoelectricity in two-dimensional group-III monochalcogenides. *Nano Research* 2015, **8**(12): 3796-3802.
24. de Jong M, *et al.* Charting the complete elastic properties of inorganic crystalline compounds. *Scientific Data* 2015, **2**(1): 150009.
25. Smidt TE, *et al.* An automatically curated first-principles database of ferroelectrics. *Scientific Data* 2020, **7**(1): 72.
26. Duerloo K-AN, Ong MT, Reed EJ. Intrinsic Piezoelectricity in Two-Dimensional Materials. *The Journal of Physical Chemistry Letters* 2012, **3**(19): 2871-2876.
27. Fei R, Li W, Li J, Yang L. Giant piezoelectricity of monolayer group IV monochalcogenides: SnSe, SnS, GeSe, and GeS. *Applied Physics Letters* 2015, **107**(17): 173104.
28. Wang H, Qian X. Two-dimensional multiferroics in monolayer group IV monochalcogenides. *2D Materials* 2017, **4**(1): 015042.
29. Xu R, Kim S-G. Figures of Merits of Piezoelectric Materials in Energy Harvesters. *PowerMEMS*. Atlanta, GA, USA; 2012.
30. Roundy S, Wright PK, Rabaey JM. *Energy Scavenging for Wireless Sensor Networks: With Special Focus on Vibrations*. Kluwer Academic Publishers, 2004.
31. Wu Y, Qiao J, Shen L, Quek SY. Manuscript in preparation.
32. Dubois M-A, Muralt P. Properties of aluminum nitride thin films for piezoelectric transducers and microwave filter applications. *Applied Physics Letters* 1999, **74**(20): 3032-3034.
33. Kamel TM, *et al.* Modeling and characterization of MEMS-based piezoelectric harvesting devices. *Journal of Micromechanics and Microengineering* 2010, **20**(10): 105023.
34. Bersuker IB. Pseudo-Jahn–Teller Effect—A Two-State Paradigm in Formation, Deformation, and Transformation of Molecular Systems and Solids. *Chemical Reviews* 2013, **113**(3): 1351-1390.
35. Yao K, Tay FEH. Measurement of longitudinal piezoelectric coefficient of thin films by a laser-scanning vibrometer. *IEEE Transactions on Ultrasonics, Ferroelectrics, and Frequency Control* 2003, **50**(2): 113-116.
36. Kalinin SV, Gruverman A. *Scanning Probe Microscopy: Electrical and Electromechanical Phenomena at the Nanoscale*. Springer New York, 2006.
37. Denning D, Guyonnet J, Rodriguez BJ. Applications of piezoresponse force microscopy in materials research: from inorganic ferroelectrics to biopiezoelectrics and beyond. *International Materials Reviews* 2016, **61**(1): 46-70.
38. Sharma P, *et al.* Orientational imaging in polar polymers by piezoresponse force microscopy. *Journal of Applied Physics* 2011, **110**(5): 052010.

39. Kim J, *et al.* Artificial creation and separation of a single vortex–antivortex pair in a ferroelectric flatland. *npj Quantum Materials* 2019, **4**(1): 29.
40. Borowiak AS, *et al.* Electromechanical response of amorphous LaAlO₃ thin film probed by scanning probe microscopies. *Applied Physics Letters* 2014, **105**(1): 012906.
41. Bark CW, *et al.* Switchable Induced Polarization in LaAlO₃/SrTiO₃ Heterostructures. *Nano Letters* 2012, **12**(4): 1765-1771.
42. Posternak M, Resta R, Baldereschi A. Role of covalent bonding in the polarization of perovskite oxides: The case of KNbO₃. *Physical Review B* 1994, **50**(12): 8911-8914.
43. You L, *et al.* Origin of giant negative piezoelectricity in a layered van der Waals ferroelectric. *Science Advances* 2019, **5**(4): eaav3780.
44. Zhang L, *et al.* Dual-Stage Nanopositioning Scheme for 10 Tbit/in² Hard Disk Drives With a Shear-Mode Piezoelectric Single-Crystal Microactuator. *IEEE Transactions on Magnetics* 2015, **51**(4): 1-9.
45. Kresse G, Furthmüller J. Efficient iterative schemes for ab initio total-energy calculations using a plane-wave basis set. *Physical Review B* 1996, **54**(16): 11169-11186.
46. Kresse G, Joubert D. From ultrasoft pseudopotentials to the projector augmented-wave method. *Physical Review B* 1999, **59**(3): 1758-1775.
47. Perdew JP, Burke K, Ernzerhof M. Generalized Gradient Approximation Made Simple. *Physical Review Letters* 1996, **77**(18): 3865-3868.
48. Mathew K, *et al.* Atomate: A high-level interface to generate, execute, and analyze computational materials science workflows. *Computational Materials Science* 2017, **139**: 140-152.
49. Jain A, *et al.* FireWorks: a dynamic workflow system designed for high-throughput applications. *Concurrency and Computation: Practice and Experience* 2015, **27**(17): 5037-5059.
50. Choudhary K, Cheon G, Reed E, Tavazza F. Elastic properties of bulk and low-dimensional materials using van der Waals density functional. *Physical Review B* 2018, **98**(1): 014107.

SUPPLEMENTARY INFORMATION

Data-driven discovery of high performance layered van der Waals piezoelectric NbOI₂

Yaze Wu^{1,2,9}, Ibrahim Abdelwahab^{2,5,9}, Ki Chang Kwon⁵, Ivan Verzhbitskiy^{1,2}, Lin Wang⁵, Weng Heng Liew⁶, Kui Yao⁶, Goki Eda^{1,2}, Kian Ping Loh^{2,5,7*}, Lei Shen^{3,4*}, Su Ying Quek^{1,2,7,8*}

¹Department of Physics, National University of Singapore, Singapore, Singapore.

²Center for Advanced 2D Materials and Graphene Research Centre, Singapore, Singapore.

³Department of Mechanical Engineering, National University of Singapore, Singapore, Singapore.

⁴Engineering Science Programme, National University of Singapore, Singapore, Singapore.

⁵Department of Chemistry, National University of Singapore, Singapore, Singapore.

⁶Institute of Materials Research and Engineering, A*STAR (Agency for Science, Technology and Research), Singapore, Singapore.

⁷NUS Graduate School, Integrative Sciences and Engineering Programme, National University of Singapore, Singapore.

⁸Department of Materials Science and Engineering, National University of Singapore, Singapore.

⁹These authors contributed equally: Yaze Wu, Ibrahim Abdelwahab.

*e-mail: chmlhkp@nus.edu.sg; shenlei@nus.edu.sg; phyqsy@nus.edu.sg

Table of Contents

Fig. S1	Plot of spontaneous polarization ($pC m^{-1}$) and maximum sheet e_{ij} for various 2D materials. -----	4
Table S1	Values of relaxed-ion e_{ij} ($10^{-10} C m^{-1}$) under different definitions. --	4
Table S2	Relaxed-ion piezoelectric tensor element (e_{ij}), piezoelectric strain tensor element (d_{ij}), and spontaneous polarization (P_i) of selected materials in units of $10^{-10} C m^{-1}$, $pm V^{-1}$ and $pC m^{-1}$ respectively. -----	5
Fig. S2	Phonon dispersion of monolayer NbOI ₂ . -----	6
Fig. S3	Energy per cell against time step for a molecular dynamics calculation performed on NbOI ₂ at 298K. -----	7
Table S3	Details of structural parameters for DFT-optimized structures of monolayer NbOX ₂ . -----	8
Table S4	Piezoelectric stress tensor elements (e_{11}) and piezoelectric strain tensor elements (d_{11}) of bulk NbOX ₂ . -----	8
Table S5	Piezoelectric tensor elements and electromechanical coupling factor of bulk NbOX ₂ . -----	9
Table S6	Dielectric constants of monolayer and bulk NbOX ₂ , computed by DFT. -----	9
Table S7	Stiffness Tensor elements C_{11} , C_{12} , C_{22} of monolayer NbOX ₂ in the unit of $N m^{-1}$ and Compliance tensor elements S_{11} , S_{12} , S_{22} , S_{66} in $m N^{-1}$. -----	10
Table S8	Summary of piezoelectric coefficients from experiments. -----	10
Table S9	Comparison between 2D and 3D piezoelectric strain moduli $ d_{ij} _{max}$ of 2D materials and their corresponding bulk piezoelectric parents. ----	11
Fig. S4	Correlation between 2D and 3D piezoelectric stress moduli $ e_{ij} _{max}$ of 2D materials and their corresponding bulk piezoelectric parents. -----	11
Table S10	Numerical values of 2D and 3D piezoelectric stress moduli $ e_{ij} _{max}$ of 2D materials and their corresponding bulk piezoelectric parents, as presented in Fig. S4. -----	12
Table S11	Details of structural parameters for bulk NbOX ₂ . -----	13
Fig. S5	Optical images of exfoliated NbOX ₂ nanosheets. -----	13
Fig. S6	PFM measurements on 82-nm-thick NbOI ₂ . -----	14
Fig. S7	PFM measurements on 23-nm-thick NbOI ₂ . -----	14
Fig. S8	PFM measurements on 98-nm-thick NbOI ₂ . -----	15
Fig. S9	PFM measurements on 4.3-nm-thick NbOI ₂ . -----	15
Fig. S10	PFM measurements on 72-nm-thick NbOCl ₂ . -----	16
Fig. S11	Vector PFM Measurements on 17.2-nm-thick NbOCl ₂ . -----	16
Fig. S12	AFM measurements on NbOX ₂ . -----	17
Fig. S13	Measurement of the piezoelectric coefficients of α -In ₂ Se ₃ and CuInP ₂ S ₆ (CIPS) using a laser scanning vibrometer (LSV). -----	17
Fig. S14	Comparison between theoretical (DFT) and experimental maximal piezoelectric strain tensor elements (d_{ij}). -----	18
Table S12	Electronic and ionic contributions to e_{11} of NbOX ₂ . -----	18

Fig. S15	Static charges on Nb and O atoms in NbOI ₂ and NbOCl ₂ , plotted as a function of δx .-----	19
Fig. S16	Integrated crystal orbital overlap population (ICOOP) for the Nb-O bond in NbOX ₂ .-----	20
Table S13	Dynamical charge ($Z_{m^x,1}^*$) and $\frac{\partial u_{m^x}}{\partial \eta_1}$ of each atom in NbOX ₂ .-----	21
Fig. S17	High-throughput calculation results for maximum out-of-plane sheet piezoelectric tensor elements.-----	21
Table S14	Materials with large e_{3j} .-----	22
Supplementary Discussions-----		22
Formalisms	-----	22
Supplementary Note 1: Polarization switching in NbOX ₂ -----		24
Fig. S18	Polar switching of NbOX ₂ -----	25
Supplementary Note 2: Ferroelectric-paraelectric phase transition in NbOI ₂	-----	26
Fig. S19	Temperature-dependent properties of NbOI ₂ .-----	26
Supplementary Note 3: Pseudo-Jahn-Teller Effect-----		27
Fig. S20	Valence and conduction band pairs involved in inducing the symmetry-breaking distortion through the PJTE.-----	27
Supplementary Note 4: Strain-assisted Ferroelectric Switching-----		28
Fig. S21	Effect of strain on the Nb-O bond lengths in NbOX ₂ .-----	28
High Throughput Calculation Results-----		29
Table S15	Table of quantities obtained from high throughput calculation workflow.-----	29
References	-----	32

I. Supplementary Tables and Figures

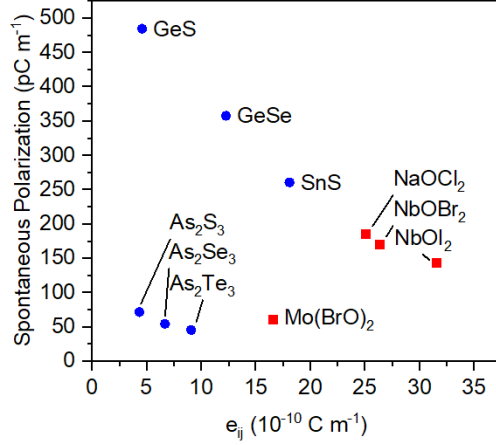


Fig. S1 | Plot of spontaneous polarization (pC m^{-1}) and maximum sheet e_{ij} for various 2D materials. Red squares denote data obtained from this study, blue dots denote data obtained from references¹⁻³.

Table S1 | Values of relaxed-ion e_{ij} ($10^{-10} \text{ C m}^{-1}$) under different definitions. RI1 and RI2 are different definitions of relaxed-ion schemes. In RI1, the e_{ij} is obtained using the Berry Phase method by straining one axis, allowing the ionic positions to relax, while not allowing the unstrained lattice vectors to relax. In RI2, the unstrained lattice is allowed to relax to account for the Poisson effect. The values of e_{ij} obtained in these schemes are compared to those obtained through DFPT and by Fei et al. We note that the Poisson effect reduces the effective e_{22} for GeSe significantly.

Material	DFPT	RI1	RI2	Ref
GeSe	12.4	12.1	~0.3	12.3 ³
SnSe	28.2	28.6	14.1	34.9 ³
NbOCl ₂	25.4	25.8	23.3	
NbOBr ₂	26.4	27.3	27.1	
NbOI ₂	31.6	33.3	31.4	

Table S2 | Relaxed-ion piezoelectric tensor element (e_{ij}), piezoelectric strain tensor element (d_{ij}), and spontaneous polarization (P_i) of selected materials in units of $10^{-10} \text{ C m}^{-1}$, pm V^{-1} and pC m^{-1} respectively. In the cases where lattice orientations used in this study is different from existing literature, indices of tensor elements from this study are used.

Material	ij	e_{ij}		d_{ij}		P_i
		This study	Other studies	This Study	Other studies	
1H-MoS ₂	11	3.72	3.64 ⁴		3.73 ⁴	
1H-MoSe ₂	11	3.84	3.92 ⁴		4.72 ⁴	
1H-WS ₂	11	2.54	2.47 ⁴		2.19 ⁴	
1H-WSe ₂	11	2.60	2.71 ⁴		2.79 ⁴	
1H-BN	11	1.46	1.38 ⁴		0.60 ⁴	
InSe	22	0.85	0.57 ⁵		1.46 ⁵	
GaS	22	1.87	1.34 ⁵		2.06 ⁵	
GaSe	22	1.79	1.47 ⁵		2.30 ⁵	
NbOCl ₂	11	25.1		27.4		185
NbOBr ₂	11	26.4		30.0		170
NbOI ₂	11	31.6		42.2		143
GeS	11		4.6 ³		75.43 ³	484 ²
GeSe	11	12.3	12.3 ³		212 ³	357 ²
SnS	11		18.1 ³		144.76 ³	260 ²
As ₂ S ₃	22	1.72	4.36 ¹		55.7 ¹	71 ¹
As ₂ Se ₃	22	3.15	6.71 ¹		61.7 ¹	54 ¹
As ₂ Te ₃			9.09 ¹		61.9 ¹	21.6 ¹
Bulk CIPS (0K DFT)	33		1.85 ⁶		18 ⁶	
Bulk CIPS (Exp)	33		36.7 ⁶		110 ⁶	

Here we note the disparity in the e_{22} values for As₂X₃ (X=S, Se) obtained in our study and those by Gao et al.¹ and attribute the disparity to the use of different exchange-correlation functionals.

In the figures below, we verify the dynamical stability of NbOI₂ by making sure there are no imaginary phonon frequencies for all **q** in the phonon dispersion spectra as well as by ensuring that there is no bond breaking in the molecular dynamics calculation.

The phonon dispersion of NbOI₂ is calculated using Quantum Espresso⁷⁻⁹ working with a Projector Augmented Wave (PAW) approach¹⁰ with the Perdew, Becke and Ernzerhof (PBE) Generalized Gradient Approximation (GGA) of the exchange-correlation functional¹¹. We use a kinetic energy cut-off of 60 Ry for the plane wave basis set and a Monkhorst-Pack k point meshes of 12×6×1 is used. The atomic coordinates are fully relaxed using the conjugate gradient scheme until the maximum energy difference between iterations is less than 10⁻¹⁴ Ry and the residual force is less than 0.0001 Ry/Bohr.

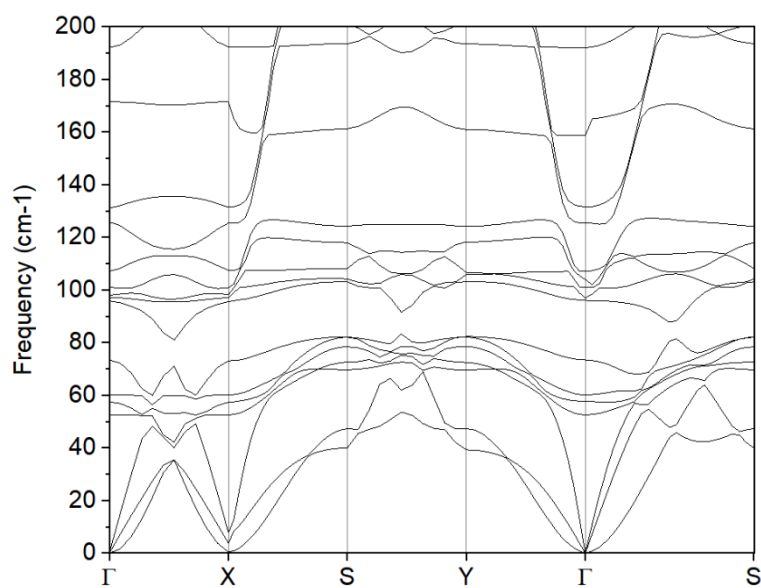


Fig. S2 | Phonon dispersion of monolayer NbOI₂. No imaginary frequency is observed, hence confirming that the structure is dynamically stable.

Ab initio molecular dynamics of NbOI₂ is performed using the VASP code¹² using the same set up as the targeted study on NbOX₂. Here, we use a 4×2×1 supercell and a Monkhorst-Pack k point mesh¹³ with a density of 3×3×1. We use the NVT ensemble at 298 K with the Nose-Hoover thermostat for 5ps and a timestep of 1fs.

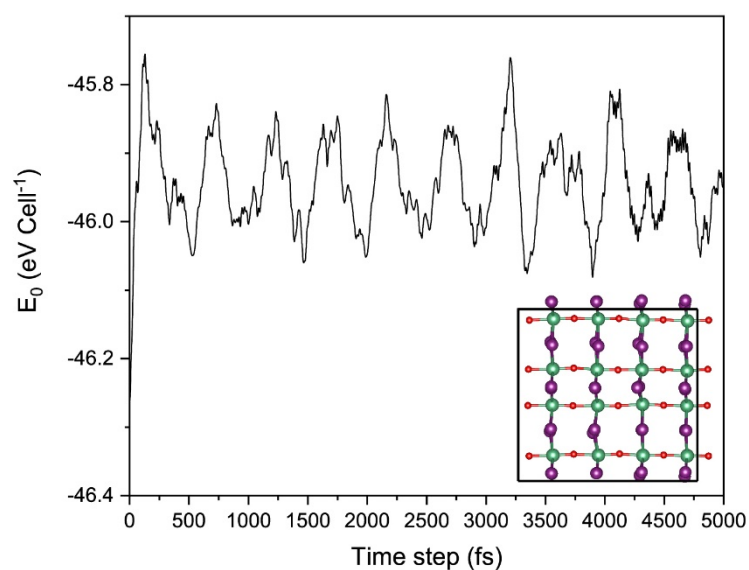


Fig. S3 | Energy per cell against time step for a molecular dynamics calculation performed on NbOI₂ at 298K. A 4×2 supercell is used for the simulation. The total energy of the system fluctuates about a fixed value, suggesting a dynamically stable structure. The inset shows the final structure after 5000 time steps of 1fs each, revealing no broken bonds, hence suggesting a dynamically stable structure at 298K.

Table S3 | Details of structural parameters for DFT-optimized structures of monolayer NbOX₂. *a* and *b* denote the in-plane lattice vectors in the polar (*x*) and non-polar (*y*) directions respectively; *l*₁ and *l*₂ are, respectively, the long and short Nb-O bond lengths in Figure 3. The magnitude of δ_x^{eqm} decreases down the halogen group with NbOCl₂ exhibiting the largest Nb displacement from the high symmetry point where $\delta x = 0 \text{ \AA}$ and NbOI₂ exhibiting the least.

	NbOCl ₂	NbOBr ₂	NbOI ₂
<i>a</i> (Å)	3.964	3.964	3.973
<i>b</i> (Å)	6.677	7.096	7.595
<i>l</i> ₁ (Å)	2.142	2.133	2.123
<i>l</i> ₂ (Å)	1.824	1.831	1.850
δ_x^{eqm} (Å)	0.318	0.302	0.274

Table S4 | Piezoelectric stress tensor elements (*e*₁₁) and piezoelectric strain tensor elements (*d*₁₁) of bulk NbOX₂. *e*₁₁ of the bulk NbOX₂ is presented in both bulk units (*C m*⁻²) as well as sheet units ($10^{-10} \text{ C m}^{-1}$), where for comparison with *e*₁₁ in the monolayer, we multiply the bulk *e*₁₁ by the cell height to obtain an equivalent sheet value.

	<i>e</i> ₁₁ (<i>C m</i> ⁻²)	sheet <i>e</i> ₁₁ ($10^{-10} \text{ C m}^{-1}$)	<i>d</i> ₁₁ (<i>pC N</i> ⁻¹)
NbOCl ₂	3.56	25.3	27.4
NbOBr ₂	3.46	26.6	30.1
NbOI ₂	3.76	31.3	42.0

Table S5 | Piezoelectric tensor elements and electromechanical coupling factor of bulk NbOX₂. Here we report values obtained from two approximations (PBE and PBE-D3) to the exchange-correlation functional.

	PBE			PBE-D3		
	NbOCl ₂	NbOBr ₂	NbOI ₂	NbOCl ₂	NbOBr ₂	NbOI ₂
e_{11} ($C m^{-2}$)	3.6	3.4	3.8	4.5	4.6	5.3
e_{12} ($C m^{-2}$)	-0.1	-0.1	-0.1	-0.2	-0.2	-0.2
e_{13} ($C m^{-2}$)	-0.1	0.0	0.0	-0.1	-0.1	-0.1
e_{26} ($C m^{-2}$)	0.1	0.1	0.1	0.1	0.1	0.1
e_{35} ($C m^{-2}$)	0.0	0.0	0.0	0.0	0.0	0.0
d_{11} ($pm V^{-1}$)	27.3	30.1	41.8	27.3	30.2	43.6
d_{12} ($pm V^{-1}$)	-4.0	-3.7	-4.7	-4.2	-4.2	-5.5
d_{13} ($pm V^{-1}$)	-16.9	-21.0	-21.7	-11.0	-10.6	-13.2
d_{26} ($pm V^{-1}$)	5.9	6.1	5.4	5.6	5.9	5.0
d_{35} ($pm V^{-1}$)	4.1	4.9	4.0	1.2	1.5	1.5
k	0.95	0.96	1.07	0.93	0.92	1.02

Table S6 | Dielectric constants of monolayer and bulk NbOX₂, computed by DFT. Values for monolayer are calculated with PBE and is scaled with respect to the thickness of the monolayer while values for bulk are calculated with both PBE and PBE-D3.

	Monolayer (PBE)			Bulk (PBE)			Bulk (PBE-D3)		
	NbOCl ₂	NbOBr ₂	NbOI ₂	NbOCl ₂	NbOBr ₂	NbOI ₂	NbOCl ₂	NbOBr ₂	NbOI ₂
ϵ_{xx}	11.9	12.5	15.7	12.1	12.6	15.5	16.2	18.4	25.0
ϵ_{yy}	11.1	11.1	11.9	11.2	11.1	12.0	13.5	13.8	14.4
ϵ_{zz}	1.9	1.9	2.0	3.2	3.5	4.2	4.3	5.1	6.3

Table S7 | Stiffness Tensor elements C_{11} , C_{12} , C_{22} of monolayer NbOX_2 in the unit of N m^{-1} and Compliance tensor elements S_{11} , S_{12} , S_{22} , S_{66} in m N^{-1} .

	C_{11}	C_{12}	C_{22}	C_{66}	S_{11}	S_{12}	S_{22}	S_{66}
NbOCl_2	92.9	5.3	62.0	15.2	10.8	-1.1	15.5	65.9
NbOBr_2	89.0	5.6	63.1	14.4	11.3	-1.0	15.9	69.2
NbOI_2	75.6	5.3	62.0	13.6	13.3	-1.1	16.2	73.5

It can be observed that the Young's Modulus along the a_x axis (i.e. C_{11}) decreases by about 19% down the halogen group from 92.9 N m^{-1} for NbOCl_2 to 75.6 N m^{-1} for NbOI_2 , while that along a_y axis (C_{22}) does not change significantly.

Table S8 | Summary of piezoelectric coefficients from experiments. The precision of the magnitudes are kept at the levels reported in the references.

Material	Piezoelectric coefficient	Magnitude	Reference
h-MoS ₂	e_{11}	$2.9 \times 10^{-10} \text{ C m}^{-1}$	14
h-BN	e_{11}	$2.91 \times 10^{-10} \text{ C m}^{-1}$	15
h-MoSSe	d_{33}	0.1 pm V^{-1}	16
WTe ₂	d_{33}	0.7 pm V^{-1}	17
g-C ₃ N ₄	d_{33}	1 pm V^{-1}	18
CdS	d_{33}	16.4 pm V^{-1}	19
SnSe	d_{11}	23 pm V^{-1}	20
ZnO nanobelt	d_{33}	$14.3 - 26.7 \text{ pm V}^{-1}$	21
α -In ₂ Se ₃	d_{33}	5.3 pm V^{-1}	This Work
CuInP ₂ S ₆	d_{33}	4.1 pm V^{-1}	This Work
NbOCl_2	d_{11}	9.4 pm V^{-1}	This Work
NbOI_2	d_{11}	21.45 pm V^{-1}	This Work

Table S9 | Comparison between 2D and 3D piezoelectric strain moduli $|d_{ij}|_{max}$ of 2D materials and their corresponding bulk piezoelectric parents. Values for 2D $|d_{ij}|_{max}$ are obtained as from **Fig. 2b**. Values of 3D $|d_{ij}|_{max}$ for InSe and GaSe are obtained from Materials Project; Values of 3D $|d_{ij}|_{max}$ for NbOX₂ are obtained from $d_{11PBE-D3}$ of **Table S5**. The materials project material ID of the parent materials are presented in square brackets.

<i>Material</i>	2D $ d_{ij} _{max}$ ($pm V^{-1}$)	3D $ d_{ij} _{max}$ ($pm V^{-1}$)
<i>InSe</i>	1.5	2.3 [mp-22691]
<i>GaSe</i>	2.3	2.9 [mp-11342] 3.3 [mp-1572]
<i>NbOCl₂</i>	27.4	27.3 [mp-549720]
<i>NbOBr₂</i>	30.0	30.2 [mp-550070]
<i>NbOI₂</i>	42.2	43.6 [mp-1025567]

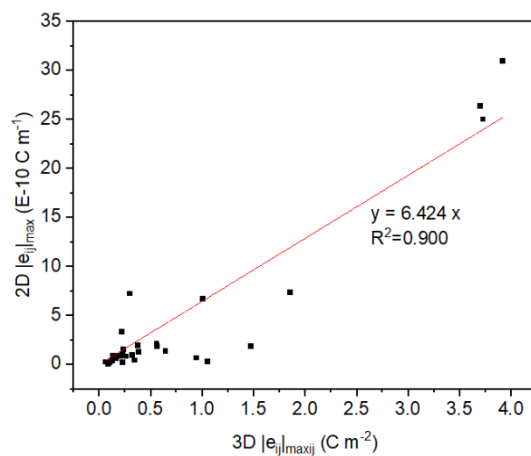


Fig. S4 | Correlation between 2D and 3D piezoelectric stress moduli $|e_{ij}|_{max}$ of 2D materials and their corresponding bulk piezoelectric parents. The linear trend line passing through the origin has a gradient of $\sim 6.4\text{\AA}$. Numerical details of each datapoint can be obtained from **Table S10**. Unlike the piezoelectric strain coefficients, the piezoelectric stress coefficients are defined differently for 2D and 3D systems, as described in the Formalisms section. The gradient of $\sim 6.4\text{\AA}$ corresponds to the average thickness of a monolayer.

Table S10 | Numerical values of 2D and 3D piezoelectric stress moduli $|e_{ij}|_{max}$ of 2D materials and their corresponding bulk piezoelectric parents, as presented in Fig. S4.

Headings of the first 3 columns are the exact database dictionary keys used in this database.

Heading of the last column is in the format MP_{dictionary_key_in_materials_project}.

<i>formula_pretty</i>	<i>mat_project_id</i>	<i>dielectric.max_abs_sheet_piezo</i> ($E-10 C m^{-1}$)	<i>MP_piezo.eij_max</i> ($C m^{-2}$)
<i>Li₂WS₄</i>	mp-753195	0.0583	0.0902
<i>Cu₂WSe₄</i>	mp-1025340	0.2071	0.2319
<i>LiBH₄</i>	mp-644223	0.2221	0.1023
<i>Cu₂WS₄</i>	mp-8976	0.2314	0.0621
<i>NaHO</i>	mp-626000	0.2808	1.0514
<i>Sn(PS₃)₂</i>	mp-36381	0.3645	0.1243
<i>H₃BrO</i>	mp-625521	0.3860	0.3468
<i>ZrCl₂</i>	mp-23162	0.6390	0.1678
<i>CaHClO</i>	mp-642725	0.6500	0.9465
<i>BiTeCl</i>	mp-28944	0.8225	0.2654
<i>InSe</i>	mp-22691	0.8475	0.1331
<i>Ta₃TeI₇</i>	mp-29117	0.8632	0.2082
<i>Nb₃SBr₇</i>	mp-29057	0.8645	0.1626
<i>Hg₃AsSe₄Br</i>	mp-567949	0.9225	0.3205
<i>Nb₃TeI₇</i>	mp-29689	0.9446	0.2286
<i>BiTeBr</i>	mp-33723	1.2412	0.3846
<i>Hg₂P₂S₇</i>	mp-27171	1.3647	0.6476
<i>B₂S₂O₉</i>	mp-1019509	1.5431	0.2371
<i>ZrGeTe₄</i>	mp-13542	1.8207	0.5666
<i>AlHO₂</i>	mp-625054	1.8717	1.4761
<i>BiTeI</i>	mp-22965	1.9007	0.3763
<i>HfGeTe₄</i>	mp-567817	2.1278	0.5587
<i>InGaS₃</i>	mp-19885	3.3485	0.2260
<i>NbTlBr₄O</i>	mp-551826	6.7080	1.0059
<i>Sn₂IF₃</i>	mp-27167	7.2032	0.3021
<i>InSnCl₃</i>	mp-998560	7.3495	1.8560
<i>NbCl₂O</i>	mp-1025567	24.9742	3.7281
<i>NbBr₂O</i>	mp-550070	26.3286	3.7007
<i>NbI₂O</i>	mp-549720	30.9221	3.9211
<i>SbF₃</i>	mp-1880	46.0720	1.5282

Table S11 | Details of structural parameters for bulk NbOX₂. DFT values are compared with those deduced from single-crystal X-ray diffraction in this work and in the ICSD database^{22, 23}. **a** and **b** denote the in-plane lattice vectors in the polar (*x*) and non-polar (*y*) directions respectively, **c** denotes the out-of-plane lattice vector; α , β and γ denote the angles $\angle\mathbf{bc}$, $\angle\mathbf{ac}$ and $\angle\mathbf{ab}$ respectively. l_1 and l_2 are, respectively, the long and short Nb-O bond lengths. The magnitude of δ_x^{eqm} decreases down the halogen group with NbOCl₂ exhibiting the largest Nb displacement from the high symmetry point where $\delta x = 0 \text{ \AA}$ and NbOI₂ exhibiting the least.

	DFT (PBE)			DFT (PBE-D3)			Experiment		ICSD	
	NbOCl ₂	NbOBr ₂	NbOI ₂	NbOCl ₂	NbOBr ₂	NbOI ₂	NbOCl ₂	NbOI ₂	NbOBr ₂	NbOI ₂
a (Å)	3.963	3.963	3.974	3.939	3.932	3.943	3.904	3.933	3.908	3.924
b (Å)	6.773	7.096	7.601	6.744	7.065	7.558	6.720	7.523	7.023	7.520
c (Å)	15.180	16.397	17.669	13.568	14.553	15.914	12.863	15.188	13.833	15.184
α (°)	104.3	105.0	105.3	105.1	105.0	104.9	105.6	105.4	105.0	105.5
β (°)	105.1	104.0	103.0	90.0	90.0	90.0	90.0	90.0	90.0	90.0
γ (°)	90.0	90.0	90.0	90.0	90.0	90.0	90.0	90.0	90.0	90.0
l_1 (Å)	2.140	2.132	2.125	2.111	2.094	2.081	2.125	2.106	2.110	2.110
l_2 (Å)	1.824	1.831	1.850	1.829	1.840	1.863	1.779	1.827	1.800	1.810
δ_x^{eqm} (Å)	0.316	0.301	0.276	0.282	0.254	0.218	0.346	0.279	0.310	0.300

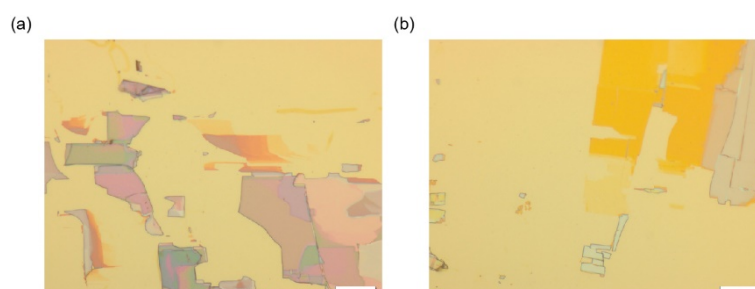


Fig. S5 | Optical images of exfoliated NbOX₂ nanosheets. (a) NbOI₂ flakes on Au substrate. (b) NbOCl₂ flakes on Au substrate.

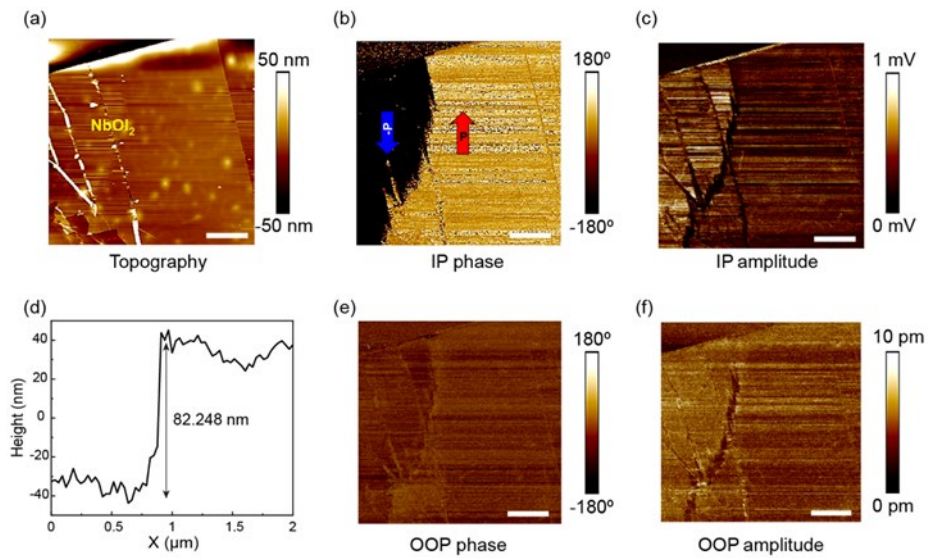


Fig. S6 | PFM measurements on 82-nm-thick NbOI₂. Topography, height profile, in-plane (IP) phase, IP amplitude, out-of-plane (OOP) phase, and OOP amplitude of 82-nm-thick NbOI₂ flake. Scale bars: 4 μm. Drive voltage: 5 V. Drive frequency: 65 kHz.

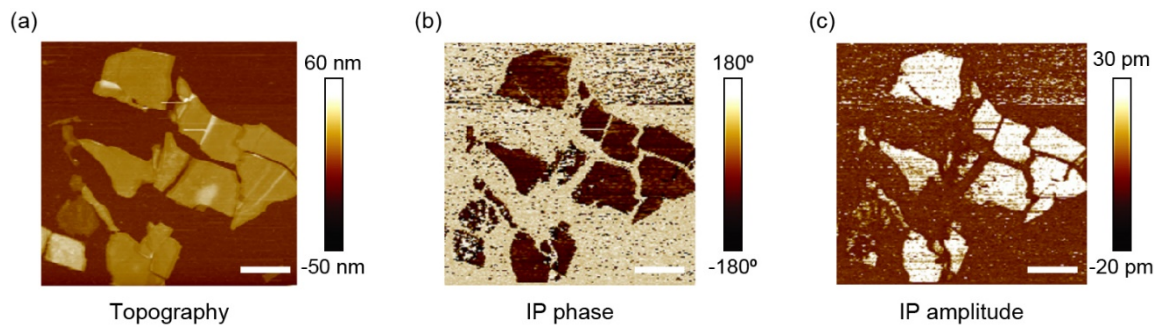


Fig. S7 | PFM measurements on 23-nm-thick NbOI₂. Topography, in-plane (IP) phase, and IP amplitude images of 23-nm-thick NbOI₂ flake. Scale bars: 4 μm. Drive voltage: 2.5 V. Drive frequency: 866 kHz.

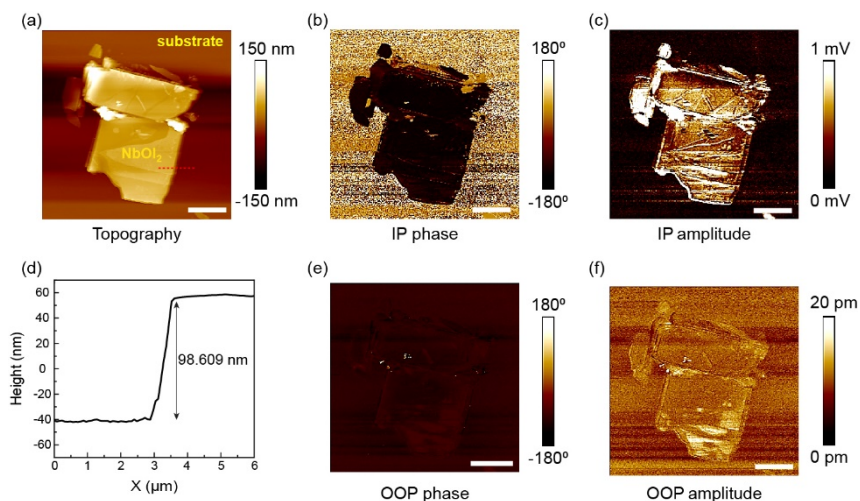


Fig. S8 | PFM measurements on 98-nm-thick NbOI₂. Topography, height profile, in-plane (IP) phase, IP amplitude, out-of-plane (OOP) phase, and OOP amplitude of 98-nm-thick NbOI₂ flake. Scale bars: 4 μm. Drive voltage: 10 V. Drive frequency: 75 kHz.

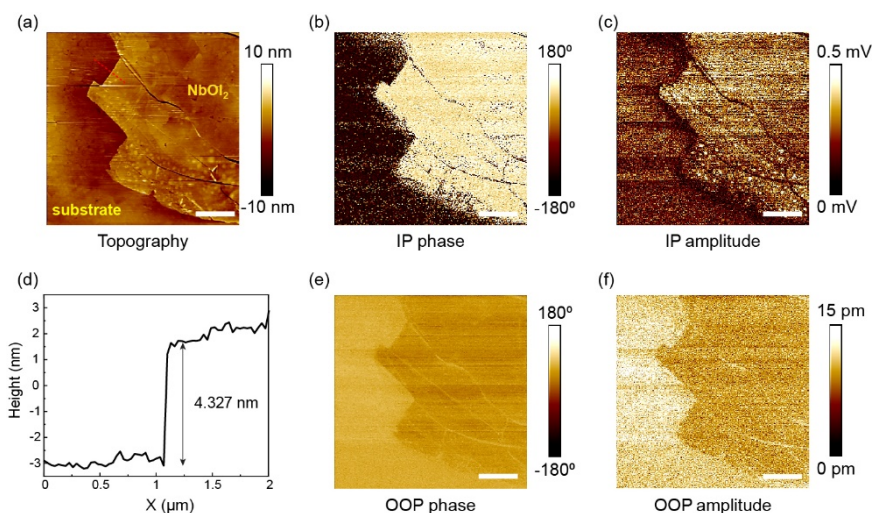


Fig. S9 | PFM measurements on 4.3-nm-thick NbOI₂. Topography, height profile, in-plane (IP) phase, IP amplitude, out-of-plane (OOP) phase, and OOP amplitude of 4.3-nm-thick NbOI₂ flake. Scale bars: 2 μm. Drive voltage: 10 V. Drive frequency: 30.5 kHz.

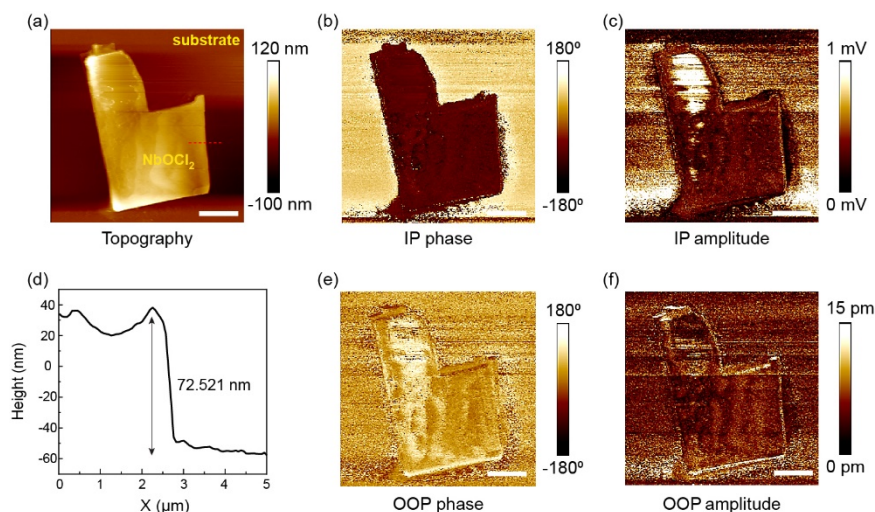


Fig. S10 | PFM measurements on 72-nm-thick NbOCl₂. Topography, height profile, in-plane (IP) phase, IP amplitude, out-of-plane (OOP) phase, and OOP amplitude of 72-nm-thick NbOCl₂ flake. Scale bars: 3 μm. Drive voltage: 10 V. Drive frequency: 75 kHz.

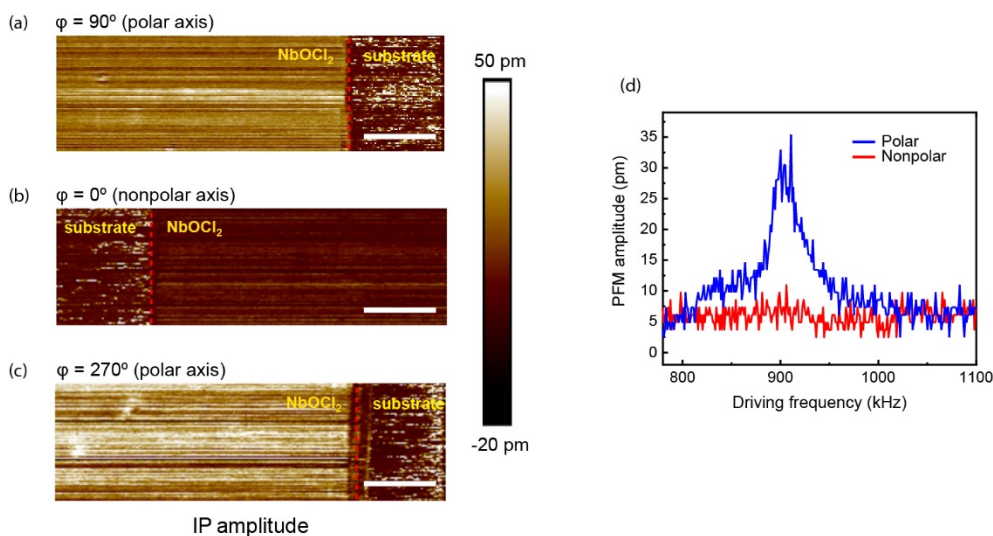


Fig. S11 | Vector PFM Measurements on 17.2-nm-thick NbOCl₂. (a-c) Vector PFM IP amplitude images of 17.2-nm-thick NbOCl₂ showing spontaneous polarization at 90° (a), 0° (b), and 270° (c) angles relative to the cantilever long axis. (d) PFM amplitude profiles along the polar and nonpolar axes of the NbOCl₂ flake. Scale bars are 2 μm.

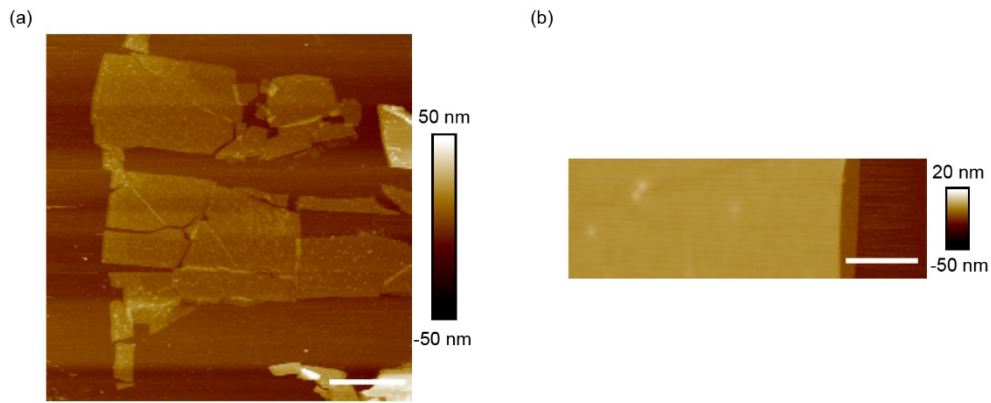


Fig. S12 | AFM measurements on NbOX₂. Topography images of (a) the 10-nm-thick NbOI₂ flakes shown in Fig. 4e-g and (b) the 17.2-nm-thick NbOCl₂ flake shown in Fig. S11. Scale bars: (a) 4 μm, (b) 2 μm.

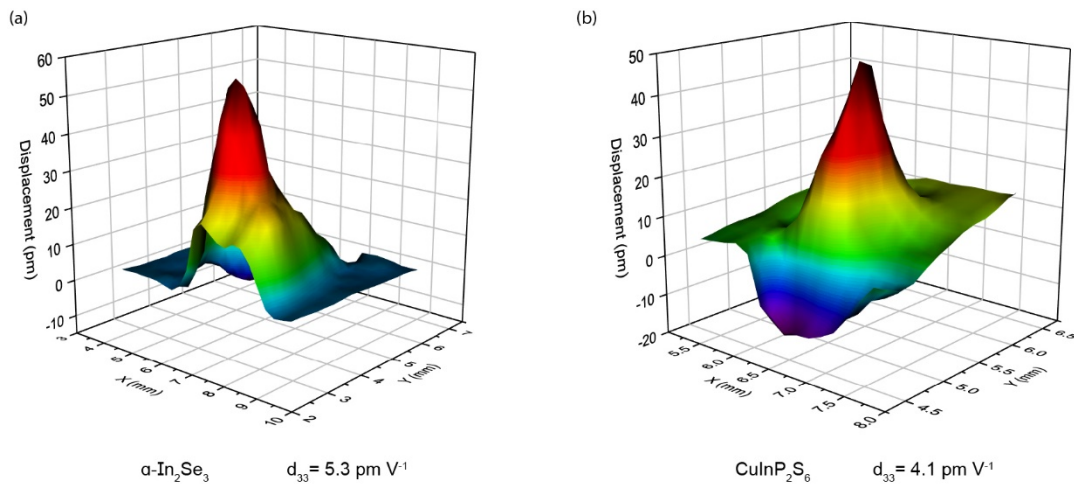


Fig. S13 | Measurement of the piezoelectric coefficients of α -In₂Se₃ and CuInP₂S₆ (CIPS) using a laser scanning vibrometer (LSV). 3D graphs of the instantaneous vibration when the displacement magnitude reaches the maximum under the sine-wave driving electrical signal. The measurements are conducted along the vertical polar directions d_{33} of α -In₂Se₃ (a) and CIPS (b). The in-plane coefficients of α -In₂Se₃ are also measured and found to be $d_{11} = 1.7$ pm/V and $d_{22} = 6.0$ pm/V.

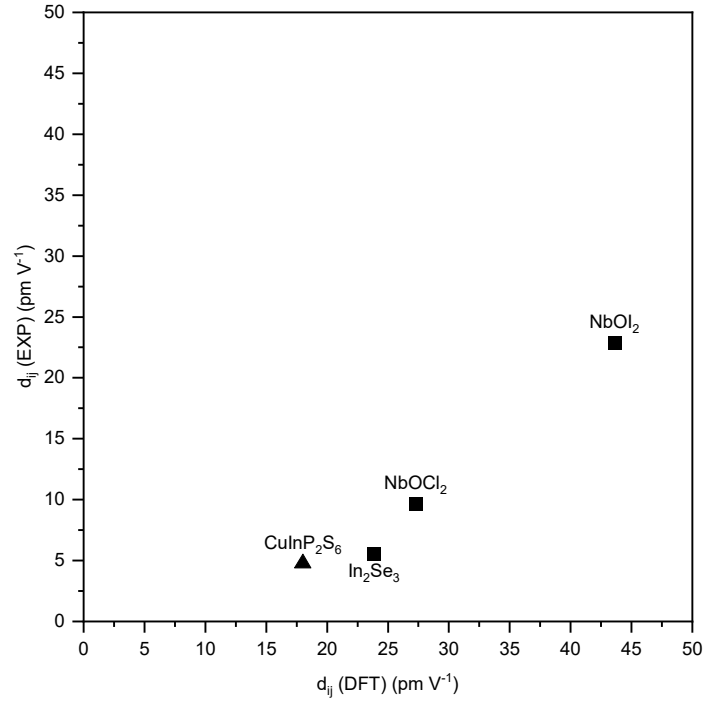


Fig. S14 | Comparison between theoretical (DFT) and experimental maximal piezoelectric strain tensor elements (d_{ij}). DFT value for d_{33} of CuInP₂S₆ is taken from ref⁶. Values for the other materials are obtained in this work. The horizontal and vertical axes of this figure are plotted in scale.

Table S12 | Electronic and ionic contributions to e_{11} of NbOX₂. The electronic contribution (e) refers to value of e_{11} computed from the “clamped ion” configuration.

e_{11}	e	ion	total
NbOCl ₂	-0.4	25.5	25.1
NbOBr ₂	-0.4	26.8	26.4
NbOI ₂	-0.2	31.8	31.6

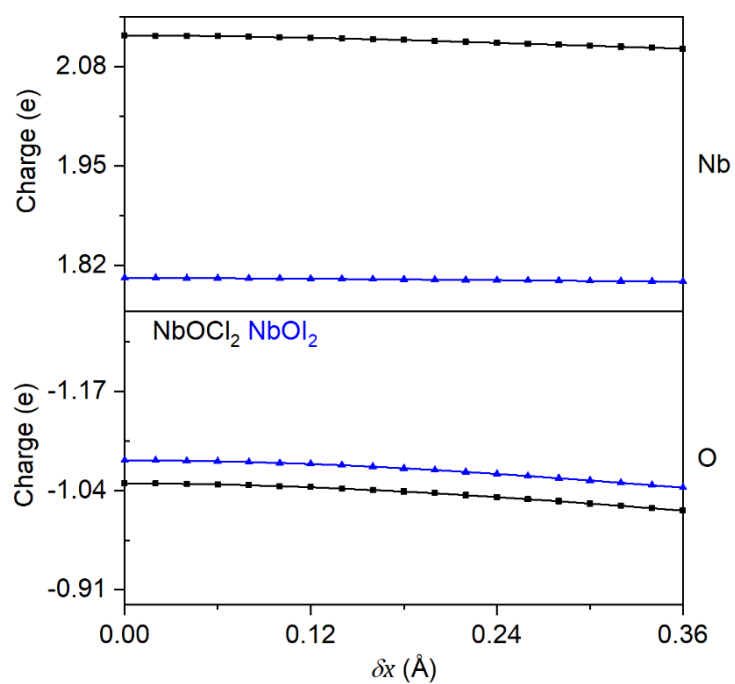


Fig. S15 | Static charges on Nb and O atoms in NbOI_2 and NbOCl_2 , plotted as a function of δx . These charges are computed using the Bader approach²⁴⁻²⁷.

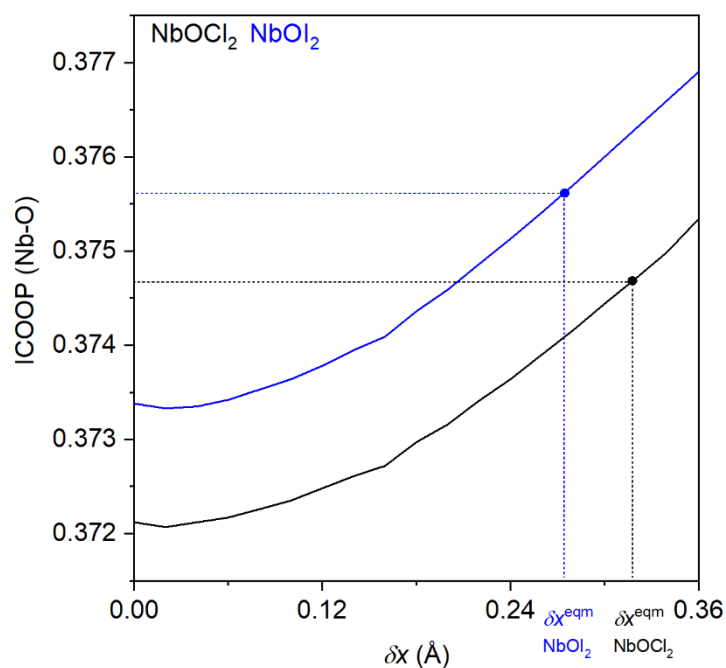


Fig. S16 | Integrated crystal orbital overlap population (ICOOP) for the Nb-O bond in NbOX_2 . ICOOP is a measure of the degree of covalency in a bond, and a more positive value indicates greater covalency²⁸. Increasing covalence in the Nb-O bond is observed as Nb is moved from the centred symmetric structure, with increasing δx . This observation is consistent with the pseudo-Jahn-Teller effect. At the same δx , Nb-O bonds are more covalent in NbOI_2 than in NbOCl_2 , which can be explained by the larger electronegativity of Cl compared to I. Dotted lines denote the values for the equilibrium structures. Nb-O bonds in NbOI_2 are more covalent than those in NbOCl_2 . The trend for NbOBr_2 falls between those of NbOI_2 and NbOCl_2 and is omitted here.

Table S13 | Dynamical charge ($Z_{m^x,1}^*$) and $\frac{\partial u_{m^x}}{\partial \eta_1}$ of each atom in NbOX₂. m^x refers to the x component of each atomic displacement. We see that the values of $Z_{m^x,1}^*$ and $\frac{\partial u_{m^x}}{\partial \eta_1}$ have the same sign, contributing to a large value in the sum for e_{11}^{ion} . Note that m^x refers to the x -component of each atomic displacement.

	$Z_{m^x,1}^*$ (e)			$\frac{\partial u_{m^x}}{\partial \eta_1}$ (Å)		
	NbOCl ₂	NbOBr ₂	NbOI ₂	NbOCl ₂	NbOBr ₂	NbOI ₂
Nb1	7.550	7.713	8.081	2.109	2.354	3.023
Nb2	7.550	7.713	8.081	2.109	2.354	3.023
X1	-0.484	-0.381	-0.218	-0.933	-1.081	-1.410
X2	-0.382	-0.274	-0.084	-0.429	-0.558	-0.844
X3	-0.382	-0.274	-0.084	-0.429	-0.558	-0.844
X4	-0.484	-0.381	-0.218	-0.933	-1.081	-1.410
O1	-6.683	-7.058	-7.779	-0.747	-0.714	-0.769
O2	-6.683	-7.058	-7.779	-0.747	-0.714	-0.769

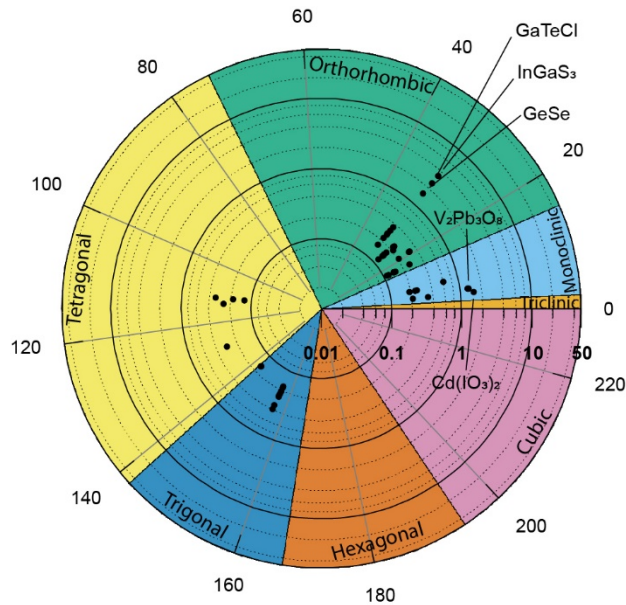


Fig. S17 | High-throughput calculation results for maximum out-of-plane sheet piezoelectric tensor elements. The radial axis represents the magnitude of e_{3j} in units of $10^{-10} \text{ C m}^{-1}$ on a log scale and the angular axis represents the 230 space groups.

Table S14 | Materials with large e_{3j} .

Material	max sheet e_{3j} (10^{-10} C m $^{-1}$)	
InGaS ₃	3.349	e_{34}
GaTeCl	2.429	e_{34}
GeSe	1.557	e_{34}
Cd(IO ₃) ₂	1.546	e_{35}
V ₂ Pb ₃ O ₈	1.330	e_{34}

II. Supplementary Discussions

Formalisms

In this section, e_{ij} refers to the three-dimensional (3D) relaxed-ion piezoelectric stress tensor, which is defined by the relation²⁹

$$e_{ij} = \left(\frac{\partial P_i}{\partial \eta_j} \right) \Big|_{\epsilon} = - \left(\frac{\partial \sigma_i}{\partial \epsilon_j} \right) \Big|_{\eta} \quad 1$$

where \mathbf{P} is the electric polarization, $\boldsymbol{\eta}$ is the homogeneous strain, $\boldsymbol{\sigma}$ is the mechanical stress, and $\boldsymbol{\epsilon}$ is the homogeneous electric field. $i = \{x, y, z\}$ and $j = \{1 \dots 6\}$ as in Voigt notation.

e_{ij} consists of two parts: clamped-ion contributions (e_{ij}^{el}) as well as ionic contributions (e_{ij}^{ion})³⁰.

$$e_{ij} = e_{ij}^{el} + e_{ij}^{ion} \quad 2$$

e_{ij}^{el} is a second-derivative response function tensor of energy (E) with respect to homogeneous electric field and homogeneous strain.

$$e_{ij}^{el} = - \frac{\partial^2 E}{\partial \epsilon_i \partial \eta_j} \Big|_u \quad 3$$

It is considered a clamped-ion quantity because the ionic coordinates (\mathbf{u}) are not relaxed when the homogeneous electric field and strain are applied, hence it represents the piezoelectric contributions from the electrons alone.

On the other hand, \mathbf{e}_{ij}^{ion} is defined, in an implied sum notation, as

$$\mathbf{e}_{ij}^{ion} = \frac{1}{\Omega_0} \mathbf{Z}_{mi}^* \frac{\partial \mathbf{u}_m}{\partial \eta_j} \quad 4$$

where Ω_0 is the cell volume before deformation and \mathbf{Z}_{mi}^* is the Born effective charge (m is a composite label for atom and displacement directions, ranging from 1 to 3N). \mathbf{e}_{ij}^{ion} represents the ionic contribution to \mathbf{e}_{ij} due to the relaxation of ionic positions after the application of strain.

\mathbf{e}_{ij} is computed using density functional perturbation theory (DFPT)³⁰⁻³² where \mathbf{e}_{ij}^{ion} is computed in terms of the pseudo inverse of force constant matrix (\mathbf{K}_{mn}) and the internal strain tensor ($\mathbf{\Lambda}_{nj}$) as shown in Equation S5)³⁰.

$$\mathbf{e}_{ij}^{ion} = \frac{1}{\Omega_0} \mathbf{Z}_{mi}^* (\mathbf{K}^{-1})_{mn} \mathbf{\Lambda}_{nj} \quad 5$$

The piezoelectric strain tensor elements (\mathbf{d}_{ij}), frequently used in experimental studies, is defined by the relation²⁹

$$\mathbf{d}_{ij} = \left(\frac{\partial \mathbf{P}_i}{\partial \sigma_j} \right) \Big|_{\epsilon} = - \left(\frac{\partial \eta_i}{\partial \epsilon_j} \right) \Big|_{\sigma} \quad 6$$

\mathbf{d}_{ij} can be obtained from \mathbf{e}_{ij} and elastic compliance tensor (\mathbf{S}_{ij}) through the following relationship

$$\mathbf{d}_{ij} = \mathbf{e}_{ik} \mathbf{S}_{kj} \quad 7$$

The sheet \mathbf{e}_{ij} defined in the main text is obtained by multiplying the 3D \mathbf{e}_{ij} by the cell height.

The sheet \mathbf{S}_{ij} defined in [Table S7](#) is obtained from 3D \mathbf{S}_{ij} by setting elements related to the z -direction to 0 and dividing the rest of the elements by cell height³³.

Using both sheet \mathbf{e}_{ij} and sheet \mathbf{S}_{ij} for calculation of \mathbf{d}_{ij} is equivalent to using their bulk counterparts because the scaling by height in both terms are cancelled off.

Note that when strain and electric field are simultaneously present, a more accurate formulation, as presented by Wu et al.³⁰, needs to be invoked. For the sake of readability, we present the “improper” formulation here while understanding that the “proper” terms as presented by Wu et al. are used in the DFPT calculations. Also, we note that the “improper” and “proper” terms are equivalent when $j = \{1, 2, 3\}$.

Supplementary Note 1: Polarization switching in NbOX₂

We study the polarization switching in bulk NbOI₂ microscopically via polarization *versus* electric field (P–E) measurements and locally through spectroscopic PFM characterizations. The P–E ferroelectric hysteresis loop of NbOI₂ when an external electric field is applied to its polar axis is displayed in [Fig. S18a](#). The polarization increases linearly with the field strength at low electrical fields, however, when the applied electric field is in the vicinity of the coercive field E_c (~ 8.5 kV/cm), the polarization shows a drastic variation due to domain reversal; the field is large enough to switch domains with the unfavorable direction of polarization. Polarization reversal is a consequence of the motion of domain walls under the influence of strong applied fields. The process involves the redistribution of the volumes of energetically favorable and unfavorable domains. The ferroelectric domain wall motion and domain switching account for the hysteretic behavior of polarization. If the applied field strength slowly decreases, some domains would back-switch. At the zero-field point, the polarization is nonzero. The crystal

reaches a zero-polarization state at the opposite E_c . Further increase of the field in the negative direction induces polarization switching in the opposite direction. The rounding of the hysteresis loop is ascribed to the small bandgap of NbOI₂ and leakage-related issues.

Scanning tip-induced switching events were recorded using spectroscopic PFM to further confirm the switching characteristics of the ultrathin NbOX₂ flakes. The local hysteresis curves of NbOI₂ and NbOCl₂ are shown in **Fig. S18b** and **Fig. S18c**, respectively. The phase-electric field hysteresis loop elucidates the local polarization behavior while the amplitude-electric field hysteresis loop defines the local strain response. We find that the phase can be switched by 180° at + 2.5 V and switched back at - 3 V, and the amplitude response displays a butterfly-like hysteric loop with dips at the same voltages as the phase curve. Meanwhile, no obvious change in the surface morphology of the NbOX₂ nanoflakes is found during the field cycling. The pronounced polarization reversibility at the positive and negative coercive field points and the corresponding butterfly strain-electric field hysteresis, affirm the polarization switching in ultrathin NbOX₂.

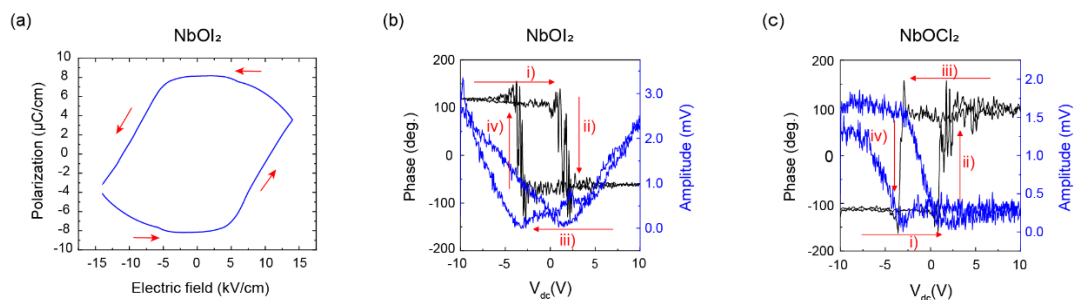


Fig. S18 | Polar switching of NbOX₂. (a) Spontaneous polarization *versus* electric field (P - E) hysteresis loop of bulk NbOI₂ sheets at room temperature. (b,c) Spectroscopic PFM switching loops of exfoliated (a) 4.1-nm-thick NbOI₂ and (b) 7.8-nm-thick NbOCl₂.

Supplementary Note 2: Ferroelectric-paraelectric phase transition in NbOI₂

The ferroelectric-paraelectric phase transition in NbOI₂ was confirmed by temperature-dependent differential scanning calorimetry (DSC) and second harmonic generation (SHG) measurements. Differential scanning calorimetry (DSC) is a thermo-analytical technique that measures physical and chemical changes within a material in response to temperature. From the DSC heat flow curve, the changes in heat capacity that occurs around the ferroelectric-paraelectric phase transition can be identified as an exothermic or endothermic peak on the low-temperature side of the material's melting/sublimation peak. **Fig. S19a** depicts the DSC result of NbOI₂ during a heating cycle. An endothermic peak with a peak value of ~ 189.27 °C is observed in the DSC heat flow curve and assigned to the phase transition Curie temperature (T_c) of NbOI₂. This corresponds to a transition from ferroelectric phase with non-centrosymmetric C2 (No. 5) symmetry to paraelectric (PE) phase with centrosymmetric C2/m (No. 12) symmetry. SHG is highly sensitive to the inversion-symmetry breaking that accompanies a ferroelectric-paraelectric phase transition; only non-centrosymmetric structures are capable of emitting SHG light. We found that the SHG signal vanishes once T_c is exceeded and emerges again upon cooling (**Fig. S19b**).

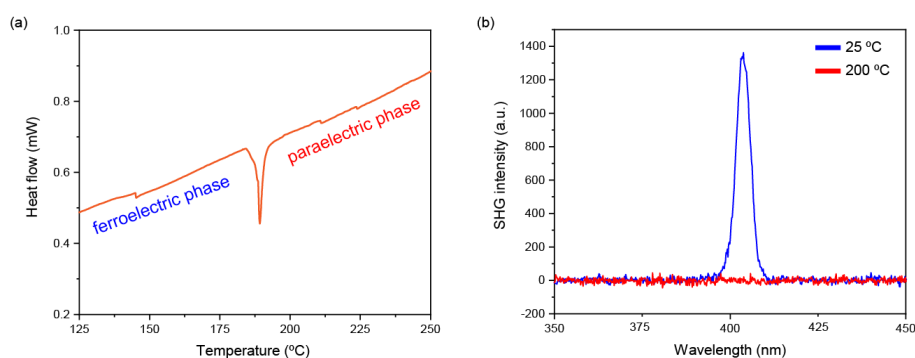


Fig. S19 | Temperature-dependent properties of NbOI₂. (a) DSC curve. (b) SHG spectra at 25 °C and 200 °C for the excitation wavelengths of $\lambda_{\text{pump}} = 800$ nm.

Supplementary Note 3: Pseudo-Jahn-Teller Effect

To understand the pseudo-Jahn-Teller effect (PJTE) driving the off-centre displacements of Nb in NbOX_2 , we construct the centred symmetric structures, in which the atoms of NbOX_2 are relaxed with the Nb atoms constrained at $\delta x = 0 \text{ \AA}$, and study the valence and conduction band eigenstates. Comparing the orbital characters of these eigenstates with those of the equilibrium structures, we identify pairs of valence and conduction band states in the equilibrium structure, that are linear combinations of pairs of valence and conduction band states in the symmetric structure. This mixing of valence and conduction band states leads to an increased covalency as well as increased energy difference within each pair of states, and is accompanied by a spontaneous symmetry-breaking distortion³⁴ as observed here. The band indices of these valence and conduction band pairs (VB1, CB1 and VB2, CB2) are provided in **Fig. S20** below. These bands mainly comprise O p_y , Nb d_{xy} , O p_z and Nb d_{xz} orbitals respectively. In both VB-CB pairs, the π -like interaction between these orbitals corroborates Wheeler et al.'s conclusion that for metals with a low d electron count, PJTE mixing of the metal d_π and X p_π orbitals favours asymmetric X-M-X bridges³⁵.

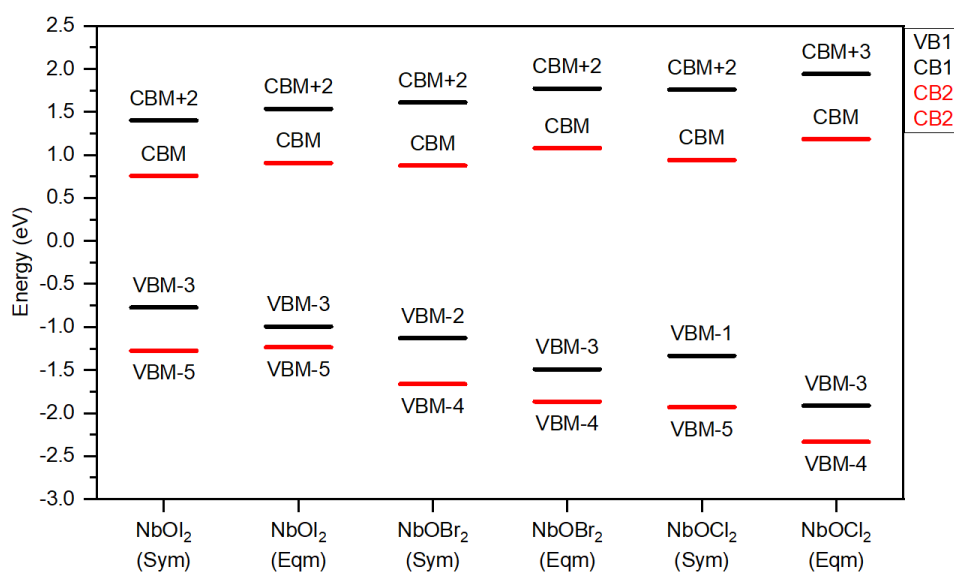


Fig. S20 | Valence and conduction band pairs involved in inducing the symmetry-breaking distortion through the PJTE. Band indices are provided at the Gamma point.

Supplementary Note 4: Strain-assisted Ferroelectric Switching

As discussed in the main text, the magnitude of the applied electric field can be much reduced if one applies compressive strain to the materials. This effect is especially large for NbOI_2 which has the largest piezoelectric effect.

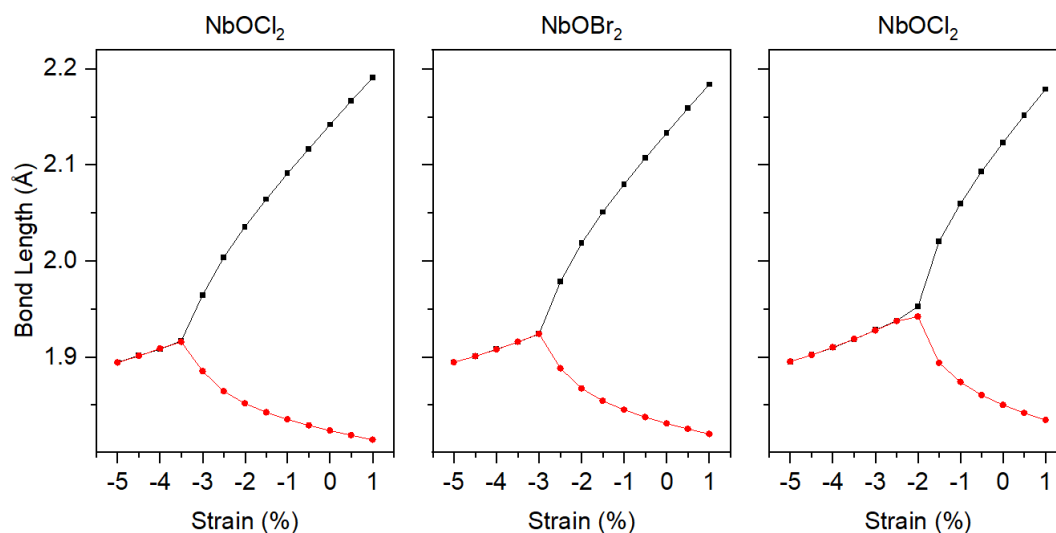


Fig. S21 | Effect of strain on the Nb-O bond lengths in NbOX_2 . A centred symmetric structure is obtained when compressive strain of over -3.5%, -3.0% and -2.5% along the x -direction is applied to NbOCl_2 , NbOBr_2 and NbOI_2 respectively.

The large response of Nb atoms in response to strain in the x -direction also enables both the magnitude of polarization and the ferroelectric switching barriers to be controlled by strain. A modest compressive strain of -2.5% in NbOI_2 results in a centred symmetric structure ([Supplementary Fig. S21](#)), allowing the polarization direction to be set with an electric field of small magnitude. The polarization magnitude can then be enhanced by applying tensile strain.

III. High Throughput Calculation Results

Table S15 | Table of quantities obtained from high throughput calculation workflow.

Formula Pretty is the human readable chemical formula of the material. **S.G. No.** is the space group number of the material. Non-ferroelectric **point groups**³⁶ are marked in bold. **Sheet plane vector direction** presents the direction of the 2D sheet's normal vector. **Height** presents the height (Å) of the unit cell. **Layer thickness** is the distance (Å), perpendicular to the 2D sheet, between the topmost and bottom most atoms. **Band gap** is in the unit of (eV). **Max abs piezo** is the magnitude of the largest piezoelectric stress tensor element in $C m^{-2}$. **Max abs sheet piezo** is the magnitude of the largest piezoelectric stress tensor element in $10^{-10} C m^{-1}$. **Max piezo index** is the index of the piezoelectric stress tensor element that has the largest magnitude. **Oop piezo** is a boolean reflecting if the material has a piezoelectric stress tensor element corresponding to the out-of-plane direction that has a magnitude larger than $0.005 C m^{-2}$. **Max abs oop piezo**, **max abs sheet oop piezo** and **max oop piezo index** are out-of-plane counterparts of Max abs piezo, max abs sheet piezo and max piezo index respectively.

formula pretty	2DMatpedia ID	S.G. No.	point group	sheet plane vector direction	height	layer thickness	band gap	max abs piezo	max abs sheet piezo	max piezo index	oop piezo	max abs oop piezo	max abs sheet oop piezo	max oop piezo index
SbF ₃	2dm-3709	31	mm2	z	23.009	2.882	4.441	TRUE	2.002	46.072	xyy	FALSE		
NbI ₂ O	2dm-4281	25	mm2	z	24.170	4.603	0.971	TRUE	1.279	30.922	xxx	FALSE		
NbBr ₂ O	2dm-4734	25	mm2	z	23.866	4.219	0.917	TRUE	1.103	26.329	xxx	FALSE		
NbCl ₂ O	2dm-3054	25	mm2	z	23.541	3.915	0.922	TRUE	1.061	24.974	xxx	FALSE		
Mo(BrO) ₂	2dm-3188	26	mm2	z	24.536	4.862	1.631	TRUE	0.678	16.626	yyy	FALSE		
GeSe	2dm-4478	31	mm2	z	23.325	2.599	1.222	TRUE	0.526	12.270	yyy	TRUE	0.067	1.557
SbAsO ₃	2dm-3790	7	m	z	22.588	4.178	4.040	TRUE	0.469	10.594	xxx	TRUE	0.010	0.232
InCu(PSe ₃) ₂	2dm-3689	149	32	z	23.339	3.424	0.503	TRUE	0.435	10.141	xyy	FALSE		
V ₂ Pb ₃ O ₈	2dm-3693	5	2	z	23.936	4.927	3.283	TRUE	0.399	9.539	yyy	TRUE	0.056	1.330
Zn(BH ₄) ₂	2dm-4877	26	mm2	z	26.663	6.255	4.499	TRUE	0.351	9.361	xyy	FALSE		
InSnCl ₃	2dm-4964	8	m	z	21.349	2.516	2.959	TRUE	0.344	7.349	xxx	FALSE		
Sn ₂ I ₃	2dm-3802	59	mmm	z	24.570	6.755	3.092	TRUE	0.293	7.203	yzx	FALSE		
NbTlBr ₄ O	2dm-3972	25	mm2	z	22.931	3.631	1.436	TRUE	0.293	6.708	xxx	FALSE		
SbTeClO ₃	2dm-4969	31	mm2	z	23.441	4.092	3.210	TRUE	0.215	5.037	yxz	TRUE	0.011	0.260
As ₂ O ₃	2dm-3779	7	m	z	22.204	3.958	4.294	TRUE	0.216	4.802	xxx	TRUE	0.011	0.246
Te ₂ Mo	2dm-5370	187	-6m2	z	23.824	3.617	1.160	TRUE	0.194	4.617	xyy	FALSE		

SrH ₂ O ₃	2dm-4166	26	mm2	z	20.896	3.923	3.054	TRUE	0.216	4.515	yyy	TRUE	0.006	0.121
TaPbF ₇	2dm-5388	6	m	z	23.050	3.270	5.255	TRUE	0.187	4.309	yyy	FALSE		
BaH ₂ O ₃	2dm-4554	26	mm2	z	25.441	3.901	3.047	TRUE	0.166	4.227	yyy	TRUE	0.006	0.148
ZnH ₂ SeO ₄	2dm-3789	7	m	z	23.395	3.932	4.458	TRUE	0.177	4.131	xyy	FALSE		
MoSe ₂	2dm-3409	187	-6m2	z	23.506	3.339	1.450	TRUE	0.163	3.839	xyy	FALSE		
MoS ₂	2dm-3150	187	-6m2	z	23.332	3.122	1.722	TRUE	0.159	3.719	yyy	FALSE		
TlBS ₃	2dm-3554	7	m	z	23.128	3.691	2.180	TRUE	0.153	3.537	yyy	TRUE	0.008	0.193
Hg ₃ SeO ₆	2dm-5414	8	m	z	21.942	2.188	1.095	TRUE	0.156	3.431	yyy	TRUE	0.028	0.609
InGaS ₃	2dm-3760	31	mm2	z	26.993	7.216	1.986	TRUE	0.124	3.349	zyz	TRUE	0.124	3.349
Te ₂ W	2dm-3050	187	-6m2	z	23.749	3.630	1.193	TRUE	0.134	3.187	yx	FALSE		
CuHgSeCl	2dm-5612	26	mm2	z	28.830	3.980	0.798	TRUE	0.110	3.181	yyy	TRUE	0.008	0.229
As ₂ Se ₃	2dm-4755	31	mm2	x	22.455	2.906	1.770	TRUE	0.141	3.158	yyy	FALSE		
WSe ₂	2dm-3594	187	-6m2	z	23.485	3.360	1.543	TRUE	0.111	2.596	xyy	FALSE		
WS ₂	2dm-3749	187	-6m2	z	23.220	3.141	1.805	TRUE	0.109	2.541	yx	FALSE		
AgBi(PSe ₃) ₂	2dm-5567	143	3	z	23.398	3.582	1.442	TRUE	0.108	2.523	yx	TRUE	0.006	0.150
GaTeCl	2dm-3523	31	mm2	z	24.660	5.327	2.296	TRUE	0.098	2.429	zyz	TRUE	0.098	2.429
SrH ₄ O ₃	2dm-3672	26	mm2	z	24.443	6.567	4.365	TRUE	0.094	2.310	yyy	TRUE	0.010	0.235
SiAs ₂	2dm-5490	26	mm2	z	25.682	6.012	1.443	TRUE	0.089	2.283	yyy	TRUE	0.006	0.154
HfGeTe ₄	2dm-4668	31	mm2	z	27.410	7.433	0.769	TRUE	0.078	2.128	yyy	FALSE		
GeAs ₂	2dm-3619	26	mm2	z	25.907	6.056	1.237	TRUE	0.080	2.073	yyy	TRUE	0.007	0.170
CuBi(PSe ₃) ₂	2dm-4194	143	3	z	23.507	3.621	1.245	TRUE	0.085	1.994	yx	TRUE	0.007	0.153
P ₂ O ₅	2dm-3519	31	mm2	z	25.403	5.462	5.080	TRUE	0.077	1.967	yyy	TRUE	0.012	0.311
HgINO ₃	2dm-3984	26	mm2	z	21.792	3.692	2.177	TRUE	0.088	1.916	yx	TRUE	0.007	0.142
BiTel	2dm-3590	156	3m	z	23.653	3.773	1.512	TRUE	0.080	1.901	yyy	TRUE	0.007	0.177
AlHO ₂	2dm-4724	31	mm2	z	25.476	5.350	4.166	TRUE	0.073	1.872	yyy	TRUE	0.014	0.354
GaS	2dm-3608	187	-6m2	z	24.524	4.643	2.396	TRUE	0.076	1.867	yyy	FALSE		
Ag ₃ SI	2dm-5200	4	2	z	29.013	9.639	0.547	TRUE	0.063	1.839	yyy	TRUE	0.012	0.339
NaTaCl ₆	2dm-3691	4	2	z	26.982	9.434	2.919	TRUE	0.068	1.821	yyy	TRUE	0.008	0.206
ZrGeTe ₄	2dm-3329	31	mm2	z	27.565	7.481	0.689	TRUE	0.066	1.821	yyy	TRUE	0.010	0.272
GaSe	2dm-3530	187	-6m2	z	24.648	4.822	1.790	TRUE	0.073	1.789	yyy	FALSE		
InAg(PSe ₃) ₂	2dm-3598	149	32	z	23.469	3.563	0.901	TRUE	0.076	1.785	yx	FALSE		
AsPO ₄	2dm-5240	31	mm2	z	25.424	4.837	4.364	TRUE	0.068	1.726	yx	FALSE		
As ₂ S ₃	2dm-4821	31	mm2	x	21.848	2.594	2.299	TRUE	0.079	1.723	yyy	FALSE		
UCO ₅	2dm-4524	25	mm2	z	23.359	3.571	2.294	TRUE	0.070	1.638	xxx	FALSE		
SiP ₂	2dm-4912	26	mm2	z	25.623	5.592	1.550	TRUE	0.063	1.609	yyy	FALSE		
VAg(PSe ₃) ₂	2dm-4708	5	2	z	23.438	3.548	0.330	TRUE	0.066	1.556	xyy	FALSE		
Cd(IO ₃) ₂	2dm-3721	4	2	z	26.236	7.374	3.531	TRUE	0.059	1.546	zzx	TRUE	0.059	1.546
B ₂ S ₂ O ₉	2dm-3130	5	2	z	26.564	7.282	6.834	TRUE	0.058	1.543	xxx	TRUE	0.048	1.273
Ca(AuF ₆) ₂	2dm-3472	115	-42m	z	23.867	7.078	1.639	TRUE	0.063	1.506	xzx	FALSE		
BN	2dm-4991	187	-6m2	z	19.935	0.000	4.711	TRUE	0.073	1.462	xyy	FALSE		
Mn(CuCl ₂) ₂	2dm-5365	25	mm2	z	20.365	2.840	0.926	TRUE	0.071	1.455	xzx	TRUE	0.010	0.213
GaAg(PSe ₃) ₂	2dm-4552	149	32	z	23.369	3.462	0.938	TRUE	0.061	1.418	yx	FALSE		
Hg ₂ P ₂ S ₇	2dm-3704	5	2	z	24.357	6.217	2.111	TRUE	0.056	1.365	xyy	FALSE		
BiTeBr	2dm-4356	156	3m	z	23.305	3.566	1.607	TRUE	0.053	1.241	xyy	FALSE		
Hg ₃ As ₄ Cl	2dm-4753	156	3m	z	22.449	3.066	2.125	TRUE	0.055	1.233	xyy	FALSE		
HfFeCl ₆	2dm-5854	5	2	z	21.980	2.939	0.241	TRUE	0.053	1.174	xyy	FALSE		
Nb ₃ Tel ₇	2dm-3841	156	3m	z	23.847	3.956	0.611	TRUE	0.040	0.945	xyy	TRUE	0.009	0.206
Hg ₃ AsSe ₄ Br	2dm-4674	156	3m	z	22.795	3.338	1.803	TRUE	0.040	0.922	yyy	FALSE		

ScAg(PS ₃) ₂	2dm-5836	149	32	z	23.162	3.358	2.045	TRUE	0.040	0.922	xyy	FALSE		
InAg(PS ₃) ₂	2dm-3602	149	32	z	23.185	3.402	1.365	TRUE	0.040	0.922	yxx	FALSE		
Ta ₃ SeI ₇	2dm-5470	156	3m	z	23.628	3.772	0.700	TRUE	0.037	0.886	yxx	TRUE	0.010	0.240
Nb ₃ SBr ₇	2dm-3765	156	3m	z	23.159	3.451	0.801	TRUE	0.037	0.865	xyy	TRUE	0.011	0.245
Ta ₃ TeI ₇	2dm-5496	156	3m	z	23.831	3.998	0.667	TRUE	0.036	0.863	yxx	TRUE	0.007	0.169
InSe	2dm-3459	187	-6m2	z	24.994	5.381	1.386	TRUE	0.034	0.848	yyy	FALSE		
LaBr ₂	2dm-5867	187	-6m2	z	23.350	3.828	0.625	TRUE	0.036	0.829	yxx	FALSE		
BiTeCl	2dm-3732	156	3m	z	23.181	3.375	1.778	TRUE	0.035	0.822	yyz	FALSE		
Nb ₃ TeCl ₇	2dm-3785	156	3m	z	23.374	3.723	0.772	TRUE	0.032	0.751	xyy	FALSE		
Ta ₃ SBr ₇	2dm-5348	156	3m	z	23.177	3.468	0.872	TRUE	0.032	0.745	yyy	TRUE	0.009	0.206
CuO ₂ F	2dm-4542	17	222	z	19.541	1.969	1.044	TRUE	0.038	0.736	yzx	FALSE		
CdTeMoO ₆	2dm-4591	113	-42m	z	27.457	7.962	3.555	TRUE	0.026	0.703	yzx	TRUE	0.009	0.244
CaHClO	2dm-4557	156	3m	z	23.101	3.583	3.598	TRUE	0.028	0.650	yyz	TRUE	0.014	0.334
ZrCl ₂	2dm-3706	187	-6m2	z	23.475	3.427	1.028	TRUE	0.027	0.639	xyy	FALSE		
MnTeMoO ₆	2dm-3666	18	222	z	27.418	7.809	2.517	TRUE	0.021	0.571	yzx	FALSE		
Ge ₃ Sb ₂ O ₉	2dm-3499	174	-6	z	23.773	4.784	3.950	TRUE	0.021	0.501	yxy	FALSE		
LaHBr ₂	2dm-4199	187	-6m2	z	23.774	3.900	3.767	TRUE	0.019	0.462	yxx	FALSE		
Hg ₃ (BO ₃) ₂	2dm-4803	189	-6m2	z	18.639	0.003	3.401	TRUE	0.024	0.452	xxx	FALSE		
Nb ₃ I ₈	2dm-5497	156	3m	z	23.975	4.058	0.233	TRUE	0.017	0.418	xyy	FALSE		
H ₃ BrO	2dm-5037	156	3m	z	21.265	1.116	5.225	TRUE	0.018	0.386	zxx	TRUE	0.018	0.386
TlAsO ₄	2dm-5146	111	-42m	z	22.060	2.087	1.492	TRUE	0.017	0.376	xyz	TRUE	0.015	0.322
Sn(PS ₃) ₂	2dm-5267	149	32	z	22.825	3.369	1.367	TRUE	0.016	0.365	yyy	FALSE		
Ag ₂ SO ₄	2dm-4885	21	222	z	20.124	1.791	2.248	TRUE	0.016	0.317	zxy	TRUE	0.016	0.317
Ag ₂ SeO ₄	2dm-3267	21	222	z	20.413	2.028	1.646	TRUE	0.015	0.311	zxy	TRUE	0.015	0.311
TmAg(PSe ₃) ₂	2dm-5578	149	32	z	23.395	3.598	1.839	TRUE	0.013	0.302	xyy	FALSE		
Nb ₃ Cl ₈	2dm-5206	156	3m	z	23.184	3.497	0.246	TRUE	0.013	0.290	yyy	FALSE		
CuSe ₂ Cl	2dm-4225	17	222	z	22.517	2.805	0.926	TRUE	0.013	0.284	yzx	TRUE	0.007	0.154
NaHO	2dm-5304	129	4/mmm	z	23.838	4.605	2.837	TRUE	0.012	0.281	zxx	TRUE	0.012	0.281
AgO ₂ F	2dm-4445	17	222	z	22.089	2.098	1.062	TRUE	0.012	0.256	zxy	TRUE	0.012	0.256
CuSe ₂ Br	2dm-4942	17	222	z	22.518	3.126	0.933	TRUE	0.011	0.248	yzx	TRUE	0.006	0.144
Cu ₂ WS ₄	2dm-4517	111	-42m	z	22.442	2.601	1.251	TRUE	0.010	0.231	xyz	TRUE	0.006	0.125
LiBH ₄	2dm-3894	156	3m	z	21.314	1.664	6.282	TRUE	0.010	0.222	zxx	TRUE	0.010	0.222
Cu ₂ SO ₄	2dm-3586	21	222	z	20.331	1.786	2.120	TRUE	0.010	0.208	zxy	TRUE	0.010	0.208
Cu ₂ WSe ₄	2dm-3107	111	-42m	z	22.514	2.839	1.233	TRUE	0.009	0.207	xyz	TRUE	0.008	0.181
LiH ₂ N	2dm-3071	113	-42m	z	23.764	3.461	3.202	TRUE	0.008	0.194	xyz	FALSE		
ScAg(PSe ₃) ₂	2dm-5821	149	32	z	23.376	3.545	1.694	TRUE	0.008	0.188	yyy	FALSE		
CuTe ₂ Br	2dm-5156	17	222	z	22.242	3.044	0.912	TRUE	0.008	0.183	yzx	TRUE	0.005	0.120
CuTe ₂ Cl	2dm-4859	17	222	z	21.769	2.749	0.886	TRUE	0.008	0.180	yzx	TRUE	0.005	0.112
AuBrO ₂	2dm-4476	17	222	z	21.615	3.040	0.963	TRUE	0.008	0.177	xyz	FALSE		
AuO ₂ F	2dm-4797	17	222	z	20.562	2.153	1.350	TRUE	0.008	0.169	yzx	FALSE		
AuClO ₂	2dm-3945	17	222	z	22.425	2.790	1.088	TRUE	0.007	0.152	xyz	FALSE		
CuTe ₂ I	2dm-5239	17	222	z	22.415	3.385	0.960	TRUE	0.006	0.144	yzx	TRUE	0.006	0.143
ErAg(PSe ₃) ₂	2dm-5480	149	32	z	23.481	3.602	1.819	TRUE	0.006	0.140	xyy	FALSE		
ZnCl ₂	2dm-4713	115	-42m	z	22.100	2.724	4.247	TRUE	0.004	0.088	zxx	FALSE		
Li ₂ WS ₄	2dm-5501	111	-42m	z	22.171	2.486	1.933	TRUE	0.003	0.058	yzx	FALSE		

IV. References

1. Gao W, Chelikowsky JR. Prediction of Intrinsic Ferroelectricity and Large Piezoelectricity in Monolayer Arsenic Chalcogenides. *Nano Letters* 2020, **20**(11): 8346-8352.
2. Wang H, Qian X. Two-dimensional multiferroics in monolayer group IV monochalcogenides. *2D Materials* 2017, **4**(1): 015042.
3. Fei R, Li W, Li J, Yang L. Giant piezoelectricity of monolayer group IV monochalcogenides: SnSe, SnS, GeSe, and GeS. *Applied Physics Letters* 2015, **107**(17): 173104.
4. Duerloo K-AN, Ong MT, Reed EJ. Intrinsic Piezoelectricity in Two-Dimensional Materials. *The Journal of Physical Chemistry Letters* 2012, **3**(19): 2871-2876.
5. Li W, Li J. Piezoelectricity in two-dimensional group-III monochalcogenides. *Nano Research* 2015, **8**(12): 3796-3802.
6. You L, *et al.* Origin of giant negative piezoelectricity in a layered van der Waals ferroelectric. *Science Advances* 2019, **5**(4): eaav3780.
7. Giannozzi P, *et al.* QUANTUM ESPRESSO: a modular and open-source software project for quantum simulations of materials. *Journal of Physics: Condensed Matter* 2009, **21**(39): 395502.
8. Giannozzi P, *et al.* Advanced capabilities for materials modelling with Quantum ESPRESSO. *Journal of Physics: Condensed Matter* 2017, **29**(46): 465901.
9. Giannozzi P, *et al.* Quantum ESPRESSO toward the exascale. *The Journal of Chemical Physics* 2020, **152**(15): 154105.
10. Blöchl PE. Projector augmented-wave method. *Physical Review B* 1994, **50**(24): 17953-17979.
11. Perdew JP, Burke K, Ernzerhof M. Generalized Gradient Approximation Made Simple. *Physical Review Letters* 1996, **77**(18): 3865-3868.
12. Kresse G, Furthmüller J. Efficient iterative schemes for ab initio total-energy calculations using a plane-wave basis set. *Physical Review B* 1996, **54**(16): 11169-11186.
13. Monkhorst HJ, Pack JD. Special points for Brillouin-zone integrations. *Physical Review B* 1976, **13**(12): 5188-5192.
14. Zhu H, *et al.* Observation of piezoelectricity in free-standing monolayer MoS₂. *Nature Nanotechnology* 2015, **10**(2): 151-155.
15. Ares P, *et al.* Piezoelectricity in Monolayer Hexagonal Boron Nitride. *Advanced Materials* 2020, **32**(1).
16. Lu A-Y, *et al.* Janus monolayers of transition metal dichalcogenides. *Nature Nanotechnology* 2017, **12**(8): 744-749.
17. Sharma P, *et al.* A room-temperature ferroelectric semimetal. *Science Advances* 2019, **5**(7): eaax5080.
18. Zelisko M, *et al.* Anomalous piezoelectricity in two-dimensional graphene nitride nanosheets. *Nature Communications* 2014, **5**(1): 4284.
19. Wang X, *et al.* Subatomic deformation driven by vertical piezoelectricity from CdS ultrathin films. *Science Advances* 2016, **2**(7): e1600209.
20. Li P, *et al.* A self-powered 2D-material sensor unit driven by a SnSe piezoelectric nanogenerator. *Journal of Materials Chemistry A* 2021, **9**(8): 4716-4723.
21. Zhao M-H, Wang Z-L, Mao SX. Piezoelectric Characterization of Individual Zinc Oxide Nanobelt Probed by Piezoresponse Force Microscope. *Nano Letters* 2004, **4**(4): 587-590.
22. Beck J, Kusterer C. Crystal Structure of NbOBr₂. *Zeitschrift für anorganische und allgemeine Chemie* 2006, **632**(14): 2193-2194.

23. Rijnsdorp J, Jellinek F. The crystal structure of niobium oxide diiodide NbOI₂. *Journal of the Less Common Metals* 1978, **61**(1): 79-82.
24. Henkelman G, Arnaldsson A, Jónsson H. A fast and robust algorithm for Bader decomposition of charge density. *Computational Materials Science* 2006, **36**(3): 354-360.
25. Tang W, Sanville E, Henkelman G. A grid-based Bader analysis algorithm without lattice bias. *Journal of Physics: Condensed Matter* 2009, **21**(8): 084204.
26. Yu M, Trinkle DR. Accurate and efficient algorithm for Bader charge integration. *The Journal of Chemical Physics* 2011, **134**(6): 064111.
27. Sanville E, Kenny SD, Smith R, Henkelman G. Improved grid-based algorithm for Bader charge allocation. *Journal of Computational Chemistry* 2007, **28**(5): 899-908.
28. Hughbanks T, Hoffmann R. Chains of trans-edge-sharing molybdenum octahedra: metal-metal bonding in extended systems. *Journal of the American Chemical Society* 1983, **105**(11): 3528-3537.
29. Kochervinskii VV. Piezoelectricity in crystallizing ferroelectric polymers: Poly(vinylidene fluoride) and its copolymers (A review). *Crystallography Reports* 2003, **48**(4): 649-675.
30. Wu X, Vanderbilt D, Hamann DR. Systematic treatment of displacements, strains, and electric fields in density-functional perturbation theory. *Physical Review B* 2005, **72**(3): 035105.
31. Baroni S, de Gironcoli S, Dal Corso A, Giannozzi P. Phonons and related crystal properties from density-functional perturbation theory. *Reviews of Modern Physics* 2001, **73**(2): 515-562.
32. Gonze X. Adiabatic density-functional perturbation theory. *Physical Review A* 1995, **52**(2): 1096-1114.
33. Choudhary K, Cheon G, Reed E, Tavazza F. Elastic properties of bulk and low-dimensional materials using van der Waals density functional. *Physical Review B* 2018, **98**(1): 014107.
34. Bersuker IB. Pseudo-Jahn–Teller Effect—A Two-State Paradigm in Formation, Deformation, and Transformation of Molecular Systems and Solids. *Chemical Reviews* 2013, **113**(3): 1351-1390.
35. Wheeler RA, *et al.* Symmetric vs. asymmetric linear M-X-M linkages in molecules, polymers, and extended networks. *Journal of the American Chemical Society* 1986, **108**(9): 2222-2236.
36. Smidt TE, *et al.* An automatically curated first-principles database of ferroelectrics. *Scientific Data* 2020, **7**(1): 72.